Materials & Design 226 (2023) 111630

Contents lists available at ScienceDirect

Materials & Design

journal homepage: www.elsevier.com/locate/matdes

Improvement of cavitation erosion resistance of structural metals by alternating magnetic field treatment

Anatolii Babutskyi [a,b], Sufyan Akram [a], Mose Bevilacqua [a], Andreas Chrysanthou [a,*], Diogo Montalvão [c], Mark J. Whiting [d], Nada Pizurova [e]

[a] School of Physics, Engineering and Computer Science, University of Hertfordshire, Hatfield AL109AB, UK
[b] G.S. Pysarenko Institute for Problems of Strength, National Academy of Sciences of Ukraine, Kyiv 01014, Ukraine
[c] Department of Design and Engineering, Faculty of Science and Technology, Bournemouth University, Poole House, Talbot Campus, Fern Barrow, Poole BH12 5BB, UK
[d] Department of Mechanical Engineering Sciences, University of Surrey, Guildford, Surrey GU2 7XH, UK
[e] Institute of Physics of Materials, Czech Academy of Sciences, Žižkova 22, CZ61662 Brno, Czech Republic

HIGHLIGHTS

- Alternating magnetic field treatment improved cavitation erosion resistance of alloys via a non-thermal effect regardless of the alloy magnetic nature.
- The treatment increased hardness by precipitation of Guinier-Preston zones and Θ'' in alloy AA2014 and κ_{IV} in nickel-aluminium bronze.
- Dislocation movement from grain boundaries led to more compressive residual stresses at the surface of EN8 steel, 70/30 brass, nickel-aluminium bronze and AA2014.

GRAPHICAL ABSTRACT

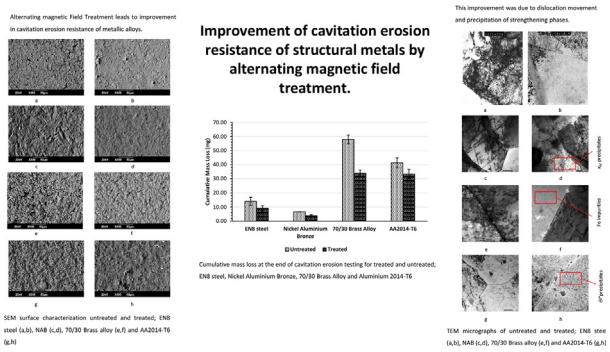

ARTICLE INFO

Article history:
Received 5 July 2022
Revised 13 January 2023
Accepted 13 January 2023
Available online 16 January 2023

Keywords:
Magnetic field treatment
Cavitation Erosion
Dislocation mobility
Precipitation

ABSTRACT

Results of cavitation erosion tests for EN8 steel, nickel-aluminium bronze (NAB), 70/30 brass and aluminium alloy AA2014-T6 following alternating magnetic field (AMF) treatment are presented. These alloys were selected because of their magnetic nature; EN8 steel is ferromagnetic, NAB and 70/30 brass are diamagnetic and AA2014 alloy is paramagnetic. The indirect cavitation erosion tests (ASTM G32–10 standard) were fulfilled at a frequency of 20 kHz in deionized water which was maintained at room temperature and ambient pressure for a predetermined time. The results show significant decrease in the mass loss for all samples that had underg1 AMF treatment. The eroded samples were characterised by means of scanning electron microscopy, while microhardness measurements showed an increase in the surface hardness as a result of the AFM treatment. The results of X-ray diffraction indicated formation of more compressive residual stresses following treatment, while examination by transmission electron microscopy showed evidence of dislocation movement away from grain boundaries. In the case of the NAB and 20014-T6 alloys, there was evidence of new precipitation. By considering the deformed state and the magnetic nature of each alloy, mechanisms explaining the increase in the cavitation erosion resistance due to the treatment are proposed and discussed.

* Corresponding author.
E-mail address: a.chrysanthou@herts.ac.uk (A. Chrysanthou).

https://doi.org/10.1016/j.matdes.2023.111630
0264-1275/

1. Introduction

Cavitation erosion is one of the most common destructive problems associated with fluid-flow systems and marine applications. Many components such as hydrofoils, valves, pumps, pipes and propellers often experience cavitation erosion damage during their service life resulting in detrimental failure and costly repair or replacement [1]. Cavitation erosion involves a combination of shock loading and fatigue processes incurred from stress generated by the repeated growth and collapse of cavities in a liquid. This phenomenon is related to the rapid formation, growth and collapse of bubbles due to the presence of strong pressure fluctuations in a liquid. Within a very short period of time, the bubbles collapse and produce shock waves on the surface of the exposed material [2]. This rapid repetition of impact induces deformation which causes micro-failure to occur followed by subsequent loss of material [3]. It has also been reported that the repetition of such pressure pulses on a solid surface can result in fatigue-like failure [4–6]. Its high economic impact has led to extensive research on cavitation erosion prevention through the use of coatings [7,8] nitriding [9] and shot-peening [10]. These techniques increase resistance against erosion by increasing surface hardness and by producing compressive residual stresses at the surface of the material without significant weight penalty [11,12]. However, some of these methods can be expensive, time-consuming and may require high levels of energy [13].

In the last 40 years, there has been growing interest in the use of external magnetic fields to improve materials properties. Studies have shown that an external magnetic field can improve fatigue resistance [14,15], microhardness [16], corrosion resistance [17] and tribological properties [18,19]. There is also evidence that the application of a magnetic field may lead to stress relief and stress relaxation [20,21]. These improvements in materials properties have been attributed to a variety of factors including changes in the dislocation density [22,23], grain refinement [24] and the generation of precipitates [14]. Research conducted by Bockstedt et al. [25] has shown that pulsed magnetic field treatment can lead to changes in the hardness and in the state of residual stresses in materials, while another study by Bataineh et al. [26] has reported the benefits of reducing the wear of cutting tools. Xi et al. [27] examined the effect of pulsed magnetic field treatment on the tribological behaviour of AISI 1045 steel and showed that the coefficient of friction decreased by 16.4 % after application of a pulsed magnetic field of 320 Gs ($320{\cdot}10^{-4}$ T) about 30 s prior to the friction wear test. These observations were attributed to increased dislocation density and refinement of ferrite. Fahmy et al. [28] reported that the fatigue life of medium carbon steel specimens that had been subjected to magnetic field treatment of 210 s at intervals of every 100,000 cycles improved fatigue life by more than two times. A recent investigation by Akram et al. [15] has shown that the use of an alternating magnetic field (AMF) resulted in substantial increase in the fatigue endurance of both EN8 steel and aluminium alloy 2014 in the T6 temper (AA2014-T6). The study also revealed a reduction of dislocation pile-up at the grain boundaries of both alloys. In addition, the treatment further generated strengthening precipitates in AA2014-T6. To the authors knowledge, the only known research work on the effect of magnetic field treatment on cavitation erosion was published in the USSR in 1991 by Snegovskii and Uvarov [29]. Full-scale tests were conducted on two hydrofoil ships of Meteor and Comet classes each equipped with two screw propellers in the treated and untreated state. The propellers used in the research had been manufactured using a cast brass (wt. %: Cu, 53 – 58; Zn, 35 – 44; Mn, 3 – 4; Fe, 0.5 – 1.5). A pulsed magnetic field of strength of 10^6 A/m was used for the treatment. The test results showed that the operating time before the appearance of surface erosion of depth of 7–8 mm for the treated propellers was 2.7 times longer. Unfortunately, the authors [29] did not provide any microstructural studies to examine the causes of the improvement in the erosion resistance.

The aim of the present study was to investigate the effect of alternating magnetic field treatment on the cavitation erosion resistance of EN8 steel, nickel-aluminium bronze (NAB), 70/30 brass and AA2014-T6 aluminium. EN8 steel is a standard load-bearing steel that is widely used in applications such as automotive components. NAB and 70/30 brass are two of the most common alloys used for marine applications due to their corrosion resistance and strength, while AA2014-T6 alloy is typically used in aerospace applications owing to its high strength-to-weight ratio. The intention of the present authors is to conduct a fundamental investigation to examine how AMF treatment affects alloys of specific magnetic nature. The alloys under investigation were selected because of their magnetic nature; the chosen alloys were ferromagnetic EN8 steel, diamagnetic NAB and 70/30 brass and paramagnetic AA2014 alloy.

2. Specimens and experimental setup

EN8 steel and nickel aluminium bronze both in the cold-rolled condition, cold drawn 70/30 brass and extruded aluminium alloy 2014 in the T6 temper were used in this investigation. The chemical compositions of EN8 steel, NAB, 70/30 brass and AA 2014-T6 are shown in Table 1.

The cavitation erosion investigation for treated and untreated alloys was carried out in compliance with the ASTM G32-10 standard [32] through a vibratory cavitation apparatus using the stationary specimen method [32,33]. The test apparatus consisted of a dedicated ultrasonic device (Vibra Sonic), which was operated at a maximum electrical peak power of 750 W and a frequency equal to 20 kHz ± 50 Hz with a vibration amplitude of 50 μm. The equipment was essentially composed of a power generator and a mechanical unit with an ultrasonic probe attached to it. The latter part of the probe was formed using a titanium waveguide (Ti-6Al-4 V). To perform the tests, the specimens were placed 0.5 mm from the horn surface. A schematic representation of the cavitation erosion system is shown in Fig. 1.

The tip of the horn was submerged in 8 mm of deionized water. As reported in the standard, this test method produces cavitation damage on the surface of the immersed specimen under high frequency vibration. The cavitation erosion test specimens were

Table 1
Nominal compositions of the alloys used in the research.

Metal	Composition, wt.%															
	Al	C	Cr	Cu	Fe	Mg	Mn	Mo	Ni	P	Pb	S	Si	Ti	Zn	Others
EN8 Steel*	–	0.36–0.44	–	–	Bal.	–	0.6–1.0	0.15	–	0.05		0.05	0.1–0.4	–	–	–
NAB**	8.5–10	–	–	Bal.	4.0–5.0	–	0.5	–	4.0–5.0	–	–0.05	–	0.1	–	0.4	0.5
70/30 Brass*	–	–	–	Bal.	0.05	–	–	–	–	–	0.07	–	–	–	28.5–31.5	0.15
AA2014-T6*	Bal.	–	0.1	3.9–5.0	0.7	0.2–0.8	0.4–1.2	–	–	–	–	–	0.5–1.2	0.15	0.25	0.15

*[30], **[31]

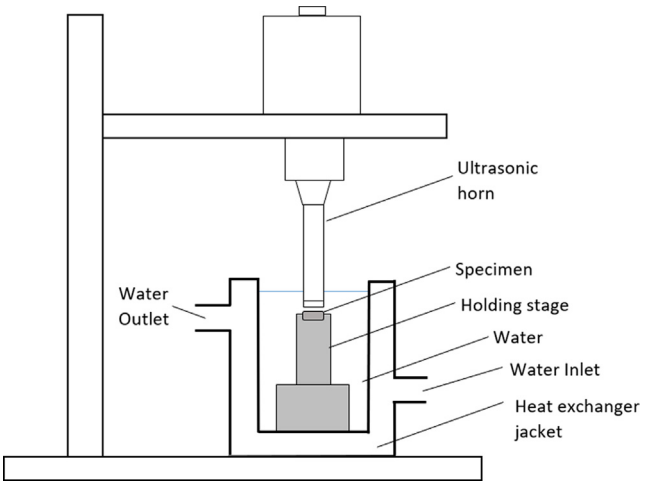

Fig. 1. Schematic diagram of the cavitation erosion test.

machined as cylinders with diameter and height of 10 mm and 5 mm respectively. Subsequently, the test surface was ground using 180, 400, 600 and 800 grit silicon carbide paper and then degreased in isopropanol in an ultrasonic bath and dried in air. Micro-hardness samples and scanning electron microscopy (SEM) samples were fine polished using 0.5 μm diamond paste.

During the cavitation tests, the holding system, specimen and horn were immersed in a thermally controlled heat jacket filled with deionised water. The tip of the horn was submerged in 8 mm of deionized water. Tests were carried out at room temperature (25 ± 2 °C). According to the standard, the tests were periodically interrupted, and samples were removed from the housing in order to measure the mass loss as a function of time. The mass loss was measured at constant intervals of 1 h up to a total investigation time of 6 h in compliance with the standard. In order to obtain reliable data, the test was performed at least twice for each sample condition and the average values were used in the subsequent analysis. For the NAB sample the cavitation erosion tests were tested up to 8 h. The mass loss due to cavitation was weighed using a precision balance (Denver Instrument). The ultrasonic horn induces the cyclic formation of very high and very low pressures [33]. This process induces the formation and collapse of cavities in the liquid which causes the cavitation erosion damage of the specimen [32,33]. Table 2 shows the initial mass of the EN8 steel, NAB, 70/30 brass alloy and AA2014-T6 cavitation erosion samples.

In order to examine the effect of the treatment on the residual stress (RS) state of the samples, RS measurements were conducted on the same sample in the untreated and treated state. RS measurements were carried out using a Bruker D8 Advance X-ray diffractometer with a Cu-Kα radiation energy of 8.05 keV (wavelength = 1.540549 Å) and Poisson's ratio, ν, of 0.33. The tube voltage and amperage were set at 40 kV and 40 mA respectively. The monochromator slit was set at 0.6 mm sample size. In measuring RS using XRD, the strain in the crystal lattice is measured and the associated RS is determined from the elastic constants assuming a linear elastic distortion of the appropriate crystal lattice plane. The method uses the diffraction angle (or d-spacing) shifts to calculate the residual stress and the LEPTOS software obtains the stress tensor at a point.

The peaks evaluated for EN8 steel, AA2014-T6, 70/30 brass and NAB were $2\Theta = 137.2°$, $2\Theta = 116.6°$, $2\Theta = 112.6°$ and $2\Theta = 115°$ respectively. The method used to calculate the RS was the Sliding Gravity method which is the preferred method for industrial products [34]. To improve the accuracy, background subtraction, smoothing, $K_{\alpha 2}$ correction, absorption correction and polarisation corrections were performed. The stress model that was used was normal stressed. All the data were analysed using the Leptos software version 7.9. The strain in the crystal lattice is measured and the associated RS is determined from the elastic constants assuming a linear elastic distortion of the appropriate crystal lattice plane. Magnetic force microscopy (MFM) using an Easyscan 2 Atomic Force Microscope (AFM) was used to detect changes in the magnetic domain structure before and after treatment for EN8 steel and NAB. A Neodynium magnet MagneticMulti74-G cantilever probe was used to scan the surface with a tip height of 60 nm. Vickers microhardness tests were performed using a Struers DuraScan microhardness tester with a load of 1 N and the load time was 15 s. Hardness values were obtained by averaging at least 60 indentations across two radii of each sample. Morphology observations of the eroded alloys (with and without treatment) were measured and compared using a JEOL JSM-5700F scanning electron microscope (SEM) operated at 20 kV. The EN8 steel, 70/30 brass and NAB samples were observed after 30 min of erosion testing and the AA2014-T6 samples were observed after 5 min of testing. Electrical conductivity tests were fulfilled for AA2014-T6 using a Foerster SIGMA TEST 2.069 electrical conductivity meter at room temperature.

Examination by transmission electron microscopy (TEM) for treated and untreated EN8 steel was performed using a FEI/Philips CM-20 operated at 200 kV. The EN8 steel TEM samples were prepared using a TESCAN LYRAS 3 equipped with a high-performance CANION FIB system for precise cross-sectioning. In the case of the NAB, AA2014-T6 and 70/30 brass alloy, electron transparent foil samples were prepared using standard mechanical thinning and electropolishing techniques. All the TEM samples were prepared from foils by sectioning from the near-surface area of the magnetically treated and untreated samples. The NAB and 70/30 brass alloy samples were examined using a JEOL JEM-1400F TEM operating at an accelerating voltage of 120 kV. In the case of AA2014-T6, the samples were examined using a JEOL JEM 2100F operating at an accelerating voltage of 200 kV.

For alternating magnetic field treatment, each specimen was placed inside a magnetiser. The magnetic field direction for the cavitation erosion samples is shown in Fig. 2a. The treatment duration lasted 30 min. An example of the registration of the magnetic field without a specimen in the magnetiser can be observed in Fig. 2b. The magnetic flux density was recorded using a Hirst GM08 Gaussmeter and the registration was conducted using a Picoscope 4224. The magnetic flux density recorded in the absence of the sample was 0.83 T. The increase in the temperature of the samples after the treatment was measured using a K-type thermocouple. The temperature rise for cavitation erosion samples are as follows: 11.7 °C for EN8 steel, 11.6 °C for 70/30 brass, 11.3 °C for NAB and 11.4 °C for AA2014-T6.

Table 2
Initial mass of cavitation erosion sample for EN8 steel, NAB, 70/30 brass alloy and AA2014-T6.

Sample	EN8 steel		NAB		70/30 Bass		AA2014-T6	
	Untreated (g)	Treated (g)	Untreated (g)	Treated (g)	Untreated (g)	Treated (g)	Untreated (g)	Treated (g)
1	3.3107	3.0073	2.9326	2.9526	3.1678	3.2416	1.3441	1.3308
2	2.9808	3.0037	3.0240	2.9759	3.1351	3.1998	1.3471	1.3177
3	3.0313	2.9971	2.9285	2.8936	3.1472	3.1177	1.3102	1.0536

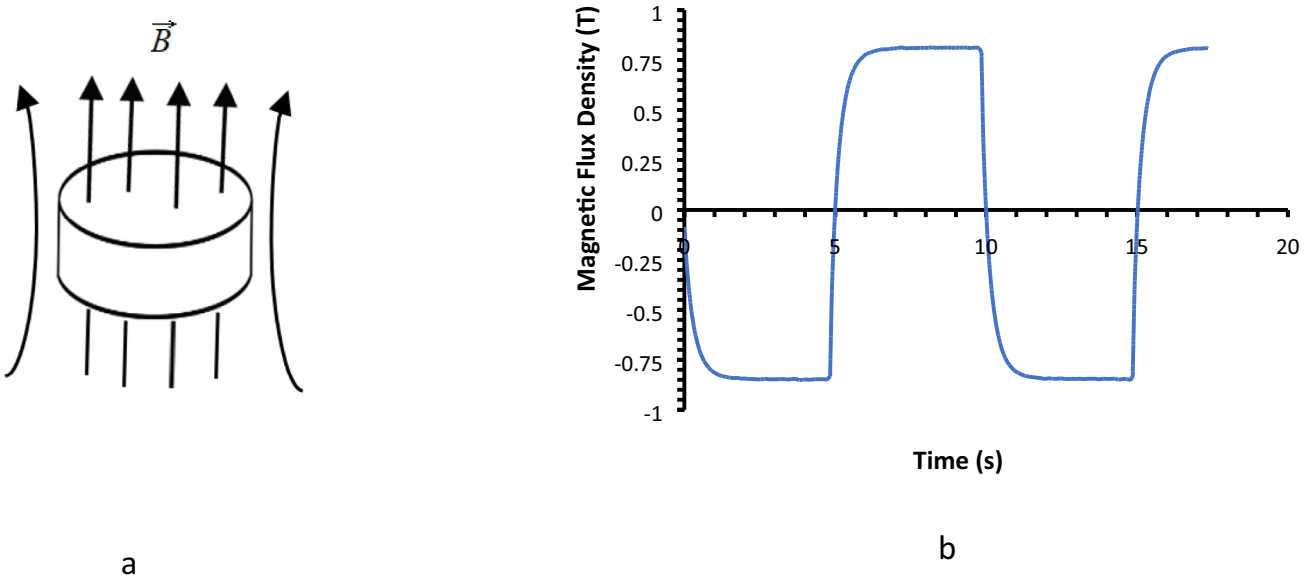

Fig. 2. Field direction relative to the sample during alternating magnetic field treatment (a) and magnetic flux density during treatment in the absence of a sample (b).

3. Results

The results of mass loss with time for EN8 steel, NAB, 70/30 brass and AA2014-T6 alloy in the untreated and AMF-treated conditions are shown in Fig. 3a, 3b, 3c and 3d respectively. The standard deviation is represented in the form of error bars in the figures. The results show that after 6 h of cavitation erosion testing, the AFM-treated EN8 steel exhibited a lower amount of mass loss by 35 % compared to the untreated condition. Similar behaviour was evident for the AMF-treated NAB, 70/30 brass and AA2014-T6 alloys; for the AMF-treated NAB, the mass loss after the test was lower by 42 % and for 70/30 brass and AA2014-T6 the value had dropped by 41 % and 20 % respectively.

The results of microhardness and RS measurements before and after treatment for all four alloys are shown in Table 3. The electrical conductivity for AA2014-T6 is also shown in Table 3. The percentage increase in microhardness after treatment for EN8 steel was 3.8 %, for NAB 4 %, for 70/30 brass 4.1 % and for AA2014-T6 4.9 % respectively. It was also observed that there was significant increase in compressive RS after treatment for all the samples. Following AMF treatment, the percentage increase in compressive RS for EN8 steel was 45.5 %, for NAB 71.7 % and for AA2014-T6 88.4 % respectively. In the case of 70/30 brass, the percentage increase in compressive RS after treatment was 173.6 %. The results also showed that there was a reduction in the electrical conductivity of the AA2014-T6 alloy of 2.4 % after treatment.

SEM micrographs of the cavitation-eroded surface for EN8 steel, NAB, 70/30 brass and AA2014-T6 in the treated and untreated conditions are presented in Fig. 4 to Fig. 7. This part of the investigation examined the behaviour of samples during the initial stages of cavitation erosion. The EN8 steel, NAB and 70/30 brass alloy samples had undergone cavitation erosion for 30 min. In the case of the AA2014-T6, SEM was conducted after testing for 5 min. From the images, it is apparent that there was more pitting and erosion in the untreated condition as compared to the AMF-treated condition. For EN8 steel, NAB and AA2014-T6, the AMF-treated condition exhibited the least amount of observed pitting and erosion as compared to the untreated condition. In the case of the 70/30 brass alloy, the morphology also revealed that the least amount erosion occurred in the AMF-treated samples. This trend is consistent with the cumulative results.

MFM results for EN8 steel before and after treatment are presented in Fig. 8a and Fig. 8b. Fig. 8c and Fig. 8d show the MFM results for untreated and treated NAB. Fig. 8b showed that there was more magnetisation and alignment of the magnetic domains as a result of the treatment. Moreover, the structure of the magnetic domains appears to be more homogeneous in the treated than in the untreated condition. Fig. 8c and Fig. 8d show that the AMF-treated NAB appears to exhibit larger and more defined areas of an attractive magnetic force gradient as opposed to the untreated condition. These observations indicate that following alternating magnetic field treatment, there appears to be more magnetisation of the magnetic domains within the material.

The brightfield TEM images for EN8 steel, NAB, 70/30 brass, and AA2014-T6 in the untreated and treated conditions are shown in Fig. 9 to Fig. 12. The results of TEM examination for an untreated EN8 steel sample in Fig. 9a show local areas of high dislocation density, including dislocation entanglement and pile-up at the grain boundaries. In the case of the AMF-treated material, redistribution of dislocations was observed to have taken place as shown in Fig. 9b. In addition, there appeared to be a reduction in the entanglement and pile up of dislocations at the grain boundaries as the concentration of the dislocations became less localised. Similar observations of dislocation redistribution, reduced dislocation entanglement and less dislocation pile-up at the grain boundaries were also observed in the treated condition for NAB, 70/30 brass and AA2014-T6 (Fig. 10 to Fig. 12). These observations provide evidence that the treatment facilitates the movement of dislocations and recovery processes.

In addition to dislocation redistribution, reduction in dislocation entanglement and reduction of dislocation pile-up at the grain boundaries, fewer stacking faults were observed in the treated NAB TEM image in Fig. 10b. The observation of a lower dislocation density implies that annihilation of dislocations had taken place as a result of the treatment. In addition, Fig. 10b shows the formation of fine κ_{IV} spherical precipitates following the treatment.

Fig. 11a and Fig. 11b show TEM images for 70/30 brass in the untreated and AMF-treated conditions respectively. Again, evidence of dislocation redistribution, reduction of dislocation entanglement and reduction of dislocation pile-up at the grain boundaries is present in the treated condition. Furthermore, order-

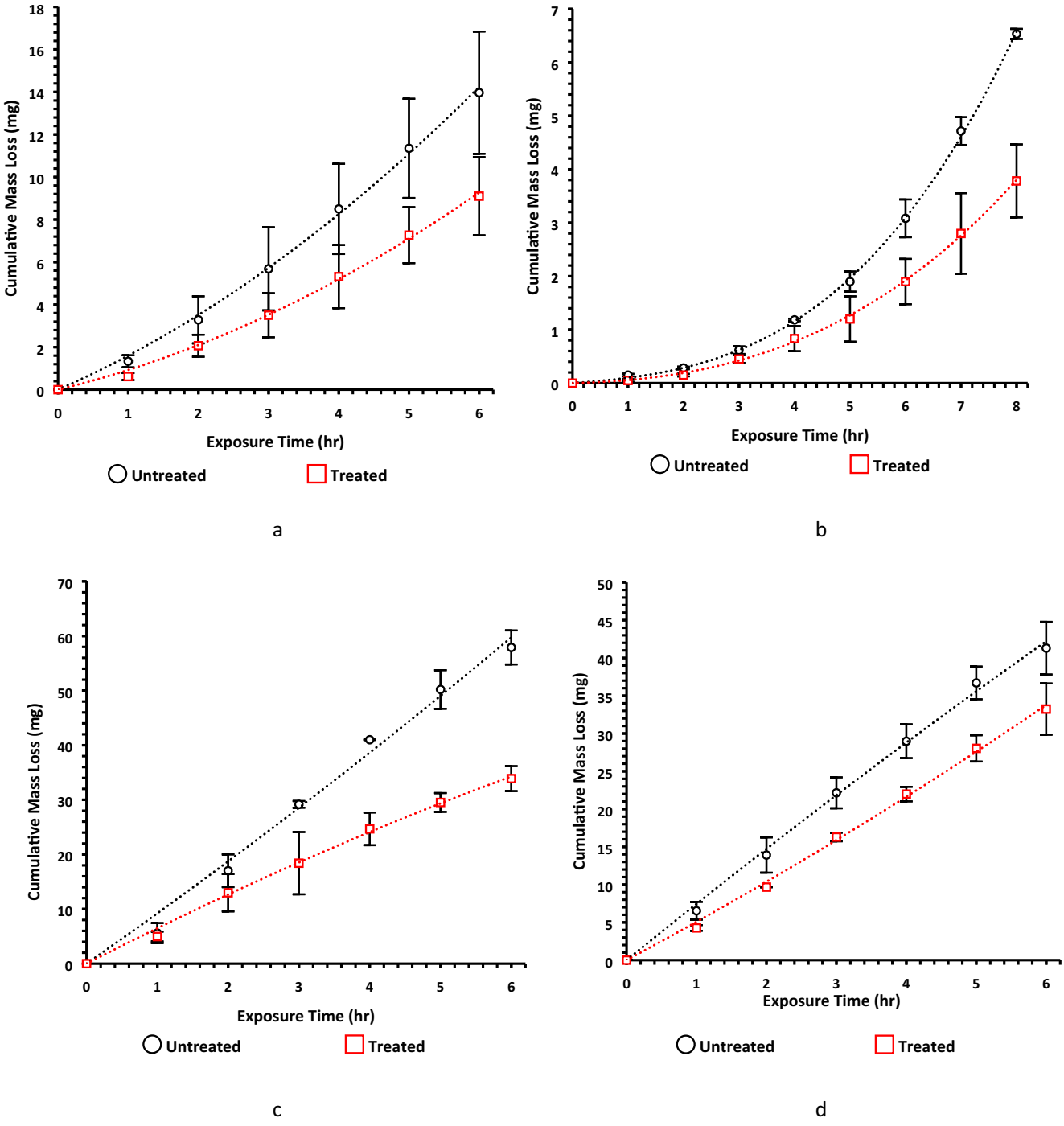

Fig. 3. Comparison of cumulative cavitation erosion rate vs time for untreated and AMF-treated EN8 Steel (a), NAB (b), 70/30 brass (c) and AA2014-T6 (d) samples.

ing of dislocations is apparent in the AMF-treated condition as well as formation of bigger clusters of Fe impurities.

Micrographs for AA2014-T6 in the untreated and AMF-treated conditions are presented in Fig. 12a and Fig. 12b. In addition to the observation of dislocation redistribution, reduction of dislocation entanglement and reduction of pile-up of dislocations at the grain boundaries in the treated condition, the presence of GP zones and theta double prime, Θ'', is more prevalent in the treated condition.

The TEM results showed evidence of new precipitates emerging in AA2014-T6 alloy and in NAB. There was no evidence of any phase transformation in the case of EN8 steel as shown in the XRD results in Fig. 13.

4. Discussion

While previous investigations [14,15,18] have demonstrated improved mechanical properties in several alloys, researchers still lack complete understanding of the effect of a magnetic field on the behaviour of metallic materials. Specifically, the effect of the magnetic nature of different alloys has not been addressed in earlier research. The present work attempts to extend current knowledge in this area by considering the response to AFM treatment of alloys that have different magnetic behaviour at room temperature; EN8 steel is ferromagnetic, AA2014 alloy is paramagnetic and the NAB and 70/30 brass are both diamagnetic. It must be noted that the NAB alloy, while being diamagnetic, it can form fine ferromagnetic

Table 3
Mean (M), Mean-square deviation (MSD) and coefficient of variation (CV) for results of microhardness, electrical conductivity and Residual stress.

Sample Condition		Microhardness[1], H_V			Electrical conductivity[2], MS/m		RS[3], MPa	
		M	MSD	CV	M	MSD	M	MSD
EN8 Steel	Untreated	265.35	6.87	0.0259	N.A.		−268.4	± 71.7
	Treated	275.33	6.82	0.0248			−319.9	± 39.0
NAB	Untreated	228.19	11.17	0.0490	N.A.		−60.4	± 28.5
	Treated	237.37	6.22	0.0262			−103.7	± 14.2
70/30 Brass	Untreated	155.29	12.9	0.0831	N.A.		37.9	± 45.5
	Treated	161.71	8.78	0.0543			−27.9	± 38.3
AA2014-T6	Untreated	155.71	4.3	0.0276	23.23	0.008	−99.3	± 40.5
	Treated	163.35	1.84	0.0113	22.67	0.017	−129.5	± 20.9

[1] average of 60 indentations per sample (3 untreated and 3 treated samples); [2] average of 20 measurements per sample (3 untreated and 3 treated samples); [3] average of 3 untreated and 3 treated samples. M is the mean; MSD is the mean-square deviation and CV is the coefficient of variation (CV = MSD/M).

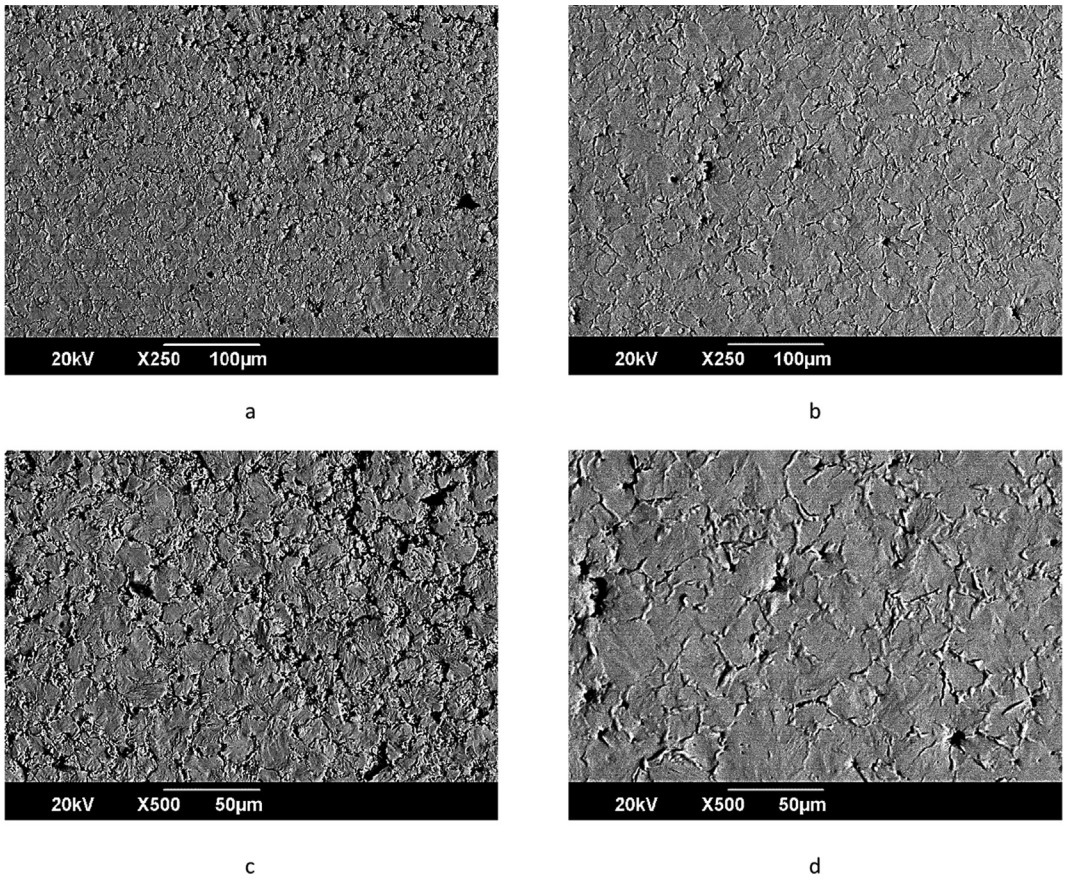

Fig. 4. SEM images at two different magnifications after 30 min of cavitation erosion for EN8 steel untreated (a and c) and AMF-treated (b and d) samples.

precipitates and so it can be described to have "soft" magnetic properties. The 70/30 brass alloy also exhibits "soft" magnetic properties in the form of ferromagnetic iron impurity particles. When discussing the mechanisms governing the observed enhancement in properties the opportunity is presented to consider whether the observed changes and improvements are universal for all metals or whether they depend on the specific magnetic nature of the alloy concerned.

The present work has shown that the four alloys which had been subjected to alternating magnetic field treatment exhibited increased resistance to cavitation erosion. The TEM results revealed that there was movement of dislocations in all four alloys as a result of alternating magnetic field treatment. In the case of the NAB bronze and the AA2014-T6 alloy there was also evidence of precipitation of strengthening phases, while coalescence of impurity iron particles was observed in 70/30 brass. The function of the magnetic field in bringing about these changes must be questioned. The most common variables that are used to describe the thermodynamic state of a material are pressure, temperature and composition. In their classic book on thermodynamics, Lewis and Randal [35] recognised the fact that other independent variables like an electric and a magnetic field can also change the thermodynamic properties of a material. A small number of theoretical studies have been undertaken to investigate the effect of magnetic fields on phase transformations. One of these few studies involving computational phase diagram predictions was carried out by Gao et al [36] and focused on the effect of magnetic fields on the α/Υ phase region in the Fe-Si system. Changes in the α/Υ temperature transition were observed as the magnetic field strength increased. The ferromagnetic α phase field was enlarged with increasing mag-

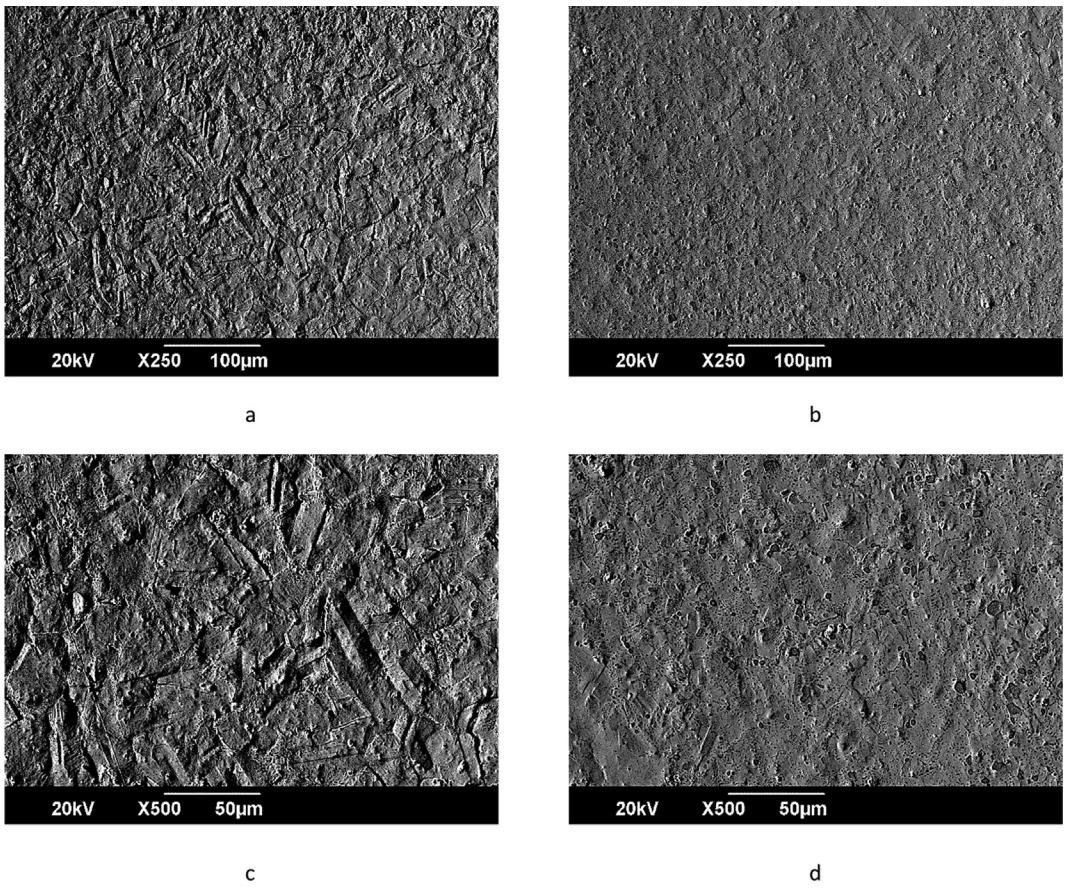

Fig. 5. SEM images at two different magnifications after 30 min of cavitation erosion for NAB untreated (a and c) and AMF-treated (b and d) samples.

netic flux density at the expense of the paramagnetic ϒ phase. From their results, it is apparent that magnetization can have a significant effect on phase transformations and that it can favour the formation of magnetic phases at the expense of non-magnetic ones. According to Gao et al [36], there is an additional contribution to the Gibbs Free energy when an external magnetic field is applied. The total free energy change, ΔG, can be presented in the form shown in equation (1)

$$\Delta G = \Delta G_{non-magnetic} + \Delta G_{magnetic(internal)} + \Delta G_{magnetic(external)} \quad (1)$$

which shows an external magnetic contribution in addition to an internal magnetic contribution and a non-magnetic contribution. The application of an external magnetic field does not affect the non-magnetic and the internal magnetic contributions, but does have an impact on the external magnetic contribution which can be calculated by equation (2)

$$\Delta G_{magnetic(external)} = -\mu \int_0^H MdH \quad (2)$$

where M is the magnetisation, H is the magnetic flux density and μ is the vacuum permeability. In the present work, the application of the alternating magnetic field to the NAB alloy has led to precipitation of the κ_{IV} phase which is based on Fe_3Al and NiAl both of which are magnetic. This additional precipitation was caused by the change in the Free energy as a result of magnetization due to the treatment. The change in the Free energy promoted the precipitation of the magnetic Fe_3Al and NiAl phases the diamagnetic copper solid solution. Under the application of the external magnetic field, the copper solid solution found itself saturated with iron and nickel as well as aluminium leading to precipitation of the κ_{IV} magnetic phases. The coalescence of the magnetic iron particles in the 70/30 brass alloy is also likely to be due to a change in the Gibbs Free energy value of the alloy as a result of magnetization. In the case of the AA2014-T6 alloy, precipitation of GP zones and *Θ"* was observed from the aluminium-copper solid solution which, at room temperature, is metastable and therefore has a small positive Gibbs Free energy in comparison to the alloy in the stable state. The transformation of the metastable solid solution to the equilibrium *Θ* ($CuAl_2$) phase is kinetically extremely slow at room temperature and requires high temperatures. At room temperature, the natural precipitation of extremely fine GP zones and *Θ"* (from the solid solution) takes place instead since the diffusion distance required for their formation is very small and thus this alloy can harden by natural ageing at room temperature. The application of the alternating magnetic field has led to additional precipitation from the metastable aluminium-copper solid solution to form GP zones and *Θ"*. Being in a metastable state, the aluminium alloy would have a small positive Gibbs Free energy and the need to lower the Free energy acts as a driving force to precipitate fine GP zones and *Θ"*. It must be noted that the level of the alternating magnetic field that was applied during the present study was not high enough to lead to precipitation of the equilibrium *Θ* ($CuAl_2$) phase.

The non-magnetic contribution to the Gibbs Free energy has led to not only chemical changes but also to changes related to stress (and strain) and to surface changes. All four alloys that were investigated were in the cold-worked state. As a metal is cold-worked by rolling, drawing or extrusion, its Gibbs Free energy increases by an amount which is approximately equal to the stored strain energy (with some energy lost as heat). This stored energy has been shown to reach up to about 60 % of the work of the initial plastic deformation at some conditions (levels and rates of plastic

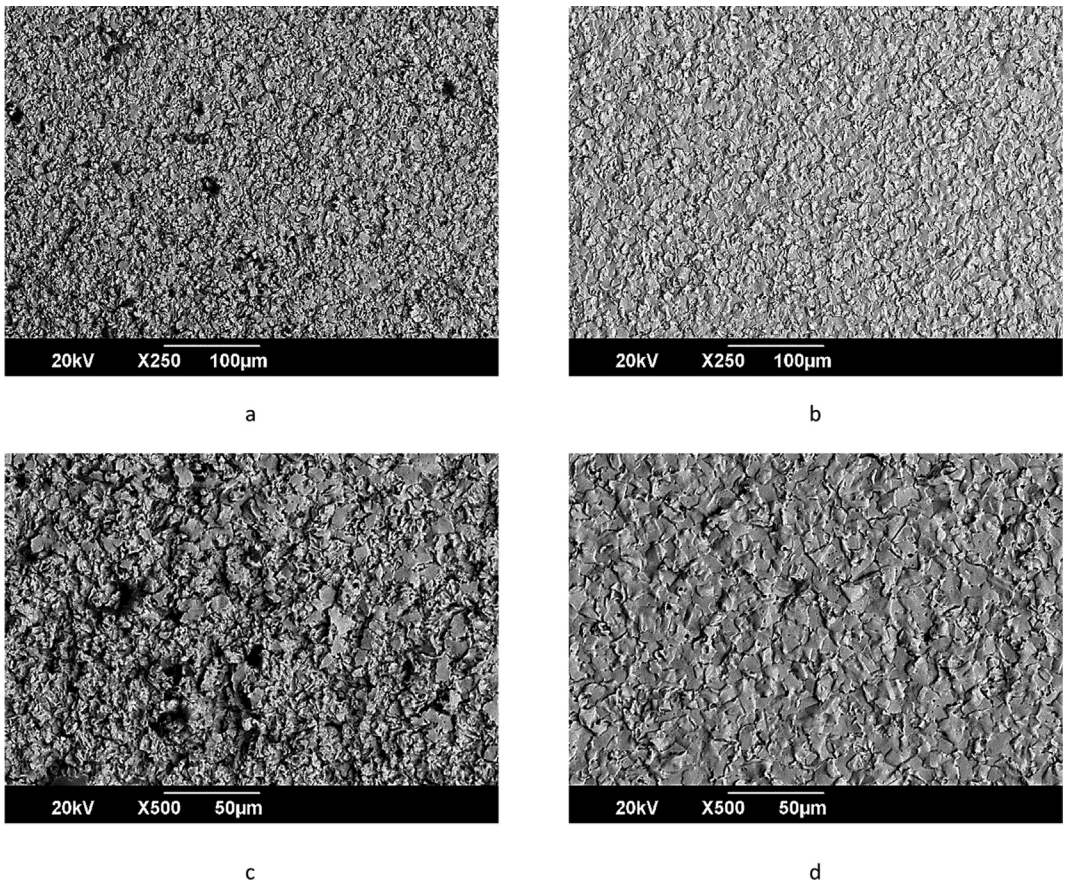

Fig. 6. SEM images at two different magnifications after 30 min of cavitation erosion for 70/30 brass alloy untreated (a and c) and AMF-treated (b and d) samples.

strain) [37,38]. When in the stressed/strained state, metals contain defects including dislocations that pile up at grain boundaries and contain residual stresses. The application of the alternating magnetic field provided the push for the four alloys to release their stored energy and thus reduce their Gibbs Free energy.

4.1. External parameters of the treatment

The present investigation has shown that the four tested alloys, irrespective of their magnetic nature, had improved resistance against cavitation erosion following the application of alternating magnetic field treatment. The observed microstructural changes involving precipitation and movement of dislocations are normally activated by heat. A common factor in the treatment with an alternating magnetic field is the fact that eddy currents are induced in the metal samples. In the present study, eddy currents were induced in each sample when the polarity of the magnetic field was changed (step change). This occurred every 5 s during the treatment process and is likely to have led to heating of the samples. A question that therefore needs to be addressed is whether the treatment has led to heating to such temperatures as to allow the observed microstructural changes. Numerical modelling of the magnetic field and eddy current distributions for each sample was carried out in order to predict the level of increase of temperature during treatment. This was undertaken by employing QuickField 6 software (Tera Analysis, Svendborg, Denmark). The solution was obtained for a 2-D formulation of a transient magnetic field problem. Fig. 14 shows a geometrical quarter model of the treatment arrangement used during numerical modelling. The physical properties of the samples and the model components used in the simulation are presented in Table 4.

The full current time variation, $I(t)$, passing through every single turn of the magnetiser windings can be presented by the equation:

$$I(t) = I_0 sign(sin(2\pi t/T)) \quad (3)$$

where T = 10 s is the period of time that the field acts in both directions during magnetisation. The value of I_0 was determined based on the best fitting of the calculated and registered profiles of the magnetic field for the magnetiser without a sample; the value that was obtained was 0.83 T (Fig. 2b).

Numerical modelling was then fulfilled for the magnetiser with samples located at the centre as illustrated in Fig. 14. According to the results, the EN8 steel sample was exposed to a magnetic flux density of about 2.95 T and the NAB sample to about 1.18 T as they were magnetised under the external magnetic field. The 70/30 brass and AA2014-T6 samples were exposed to a magnetic flux density of 0.83 T due to having a relative permeability of 1. Switching the polarity of the magnetic field gives a total change of magnetic flux density of 5.9 T and 2.36 T for the EN8 steel and NAB samples respectively. In the case of both 70/30 brass and AA2014-T6, the total change of the magnetic flux density was 1.66 T. This magnetic field variation occurred every 5 s and induced eddy currents in the samples; an example of the eddy current induced in the edge point of AA2014-T6 sample is presented in Fig. 15a which shows the distribution of the maximum eddy current vs radius on a flat surface of the samples. As shown in Fig. 15b, the maximum current density values of the resulting eddy current at the edge of the cylindrical surface of the samples was 1.22×10^6 A/m^2, 2.92×10^6 A/m^2, 0.61×10^6 A/m^2 and 4.63×10^6 A/m^2 for EN8 steel, 70/30 brass, NAB and AA2014-T6 respectively.

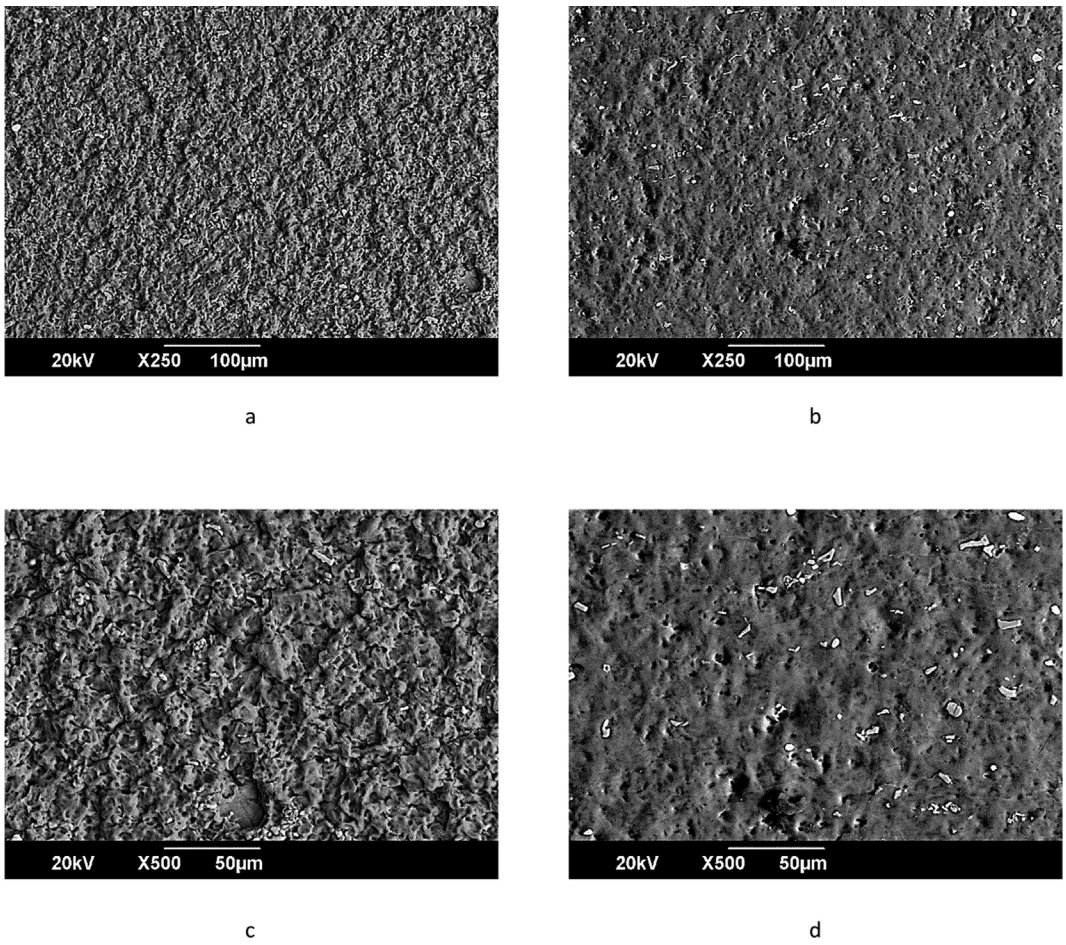

Fig. 7. SEM images at two different magnifications after 5 min of cavitation erosion for AA2014-T6 untreated (a and c) and AMF-treated (b and d) samples.

The spacers were slightly thicker than the sample geometry (see Fig. 14), preventing mutual attraction between the cores. The results showed that the temperature increase as a result of the eddy current was very small (about 11.5 °C) and in very good agreement with the experimentally measured data that were reported at the end of Section 2; such a low temperature increase is unlikely to induce the kind of changes observed, that is, movement of dislocations and to the formation of precipitates. For this reason, it can be concluded that temperature can be ruled out as a factor leading to the observed microstructural changes and that the effect was athermal.

4.2. Microstructural changes enhancing erosion resistance and their driving mechanisms.

In the present investigation, two types of microstructural changes were detected as a result of alternating magnetic field treatment. The first one is the movement and redistribution of dislocations. All four investigated metals showed reduction of dislocation density at the grain boundaries as presented in Figs. 9 - 12 with high-density dislocation structures such as dislocation tangles and pile-ups annihilating and dispersing following the treatment. The second group of changes involve precipitation of secondary phases; in the case of NAB, there was evidence of more κ_{IV} precipitates (Fig. 10b), while precipitation of Θ" occurred in the AA2014-T6 samples (Fig. 12b). These precipitates are key strengthening phases in these two alloys. In addition, there was coalescence of Fe clusters in 70/30 brass (Fig. 11b). The most probable mechanism of the movement, dispersion and redistribution of dislocations away from grain boundaries is their increased mobility which was stimulated by the treatment; this led to the mutual annihilation of dislocations of opposite sign. While grain boundaries can act as typical areas of obstruction to dislocation motion, they seem to be relatively clear of dislocations after treatment. Another natural sink for dislocations is the outer free surface (boundaries) of the samples. Treatment-stimulated dislocations from below the alloy surface were observed to easily move towards the surface. The existence of this mechanism has been confirmed experimentally by Vdovin and Kasumov [40]. In a unique experiment that they conducted, an electric current was passed through a copper foil that had been placed in a TEM. When the electric current was switched on, these researchers [40] recorded dislocation movement from the depth of the sample towards its surface where the dislocations disappeared. As this natural movement of dislocations takes place towards the surface, the accumulation of micro-strains in the subsurface regions is likely leading to an increase in surface compressive RS and, as a consequence, an increase in hardness [41,42] (see Table 3). The resulting beneficial effect of compressive RS in improving cavitation erosion resistance is well known [43,44]. In addition, secondary precipitation of κ_{IV} and Θ" phases in NAB and AA2014-T6 respectively also enhance the hardness and strength (see Table 3) of these alloys and increase their resistance to cavitation erosion. A similar effect appears to have taken place by the formation of iron clusters in 70/30 brass.

In the case of aluminium AA2014 and the NAB alloy, the movement of dislocations and the increased diffusivity of elements from solid solutions (to form precipitates) as a result of the treatment

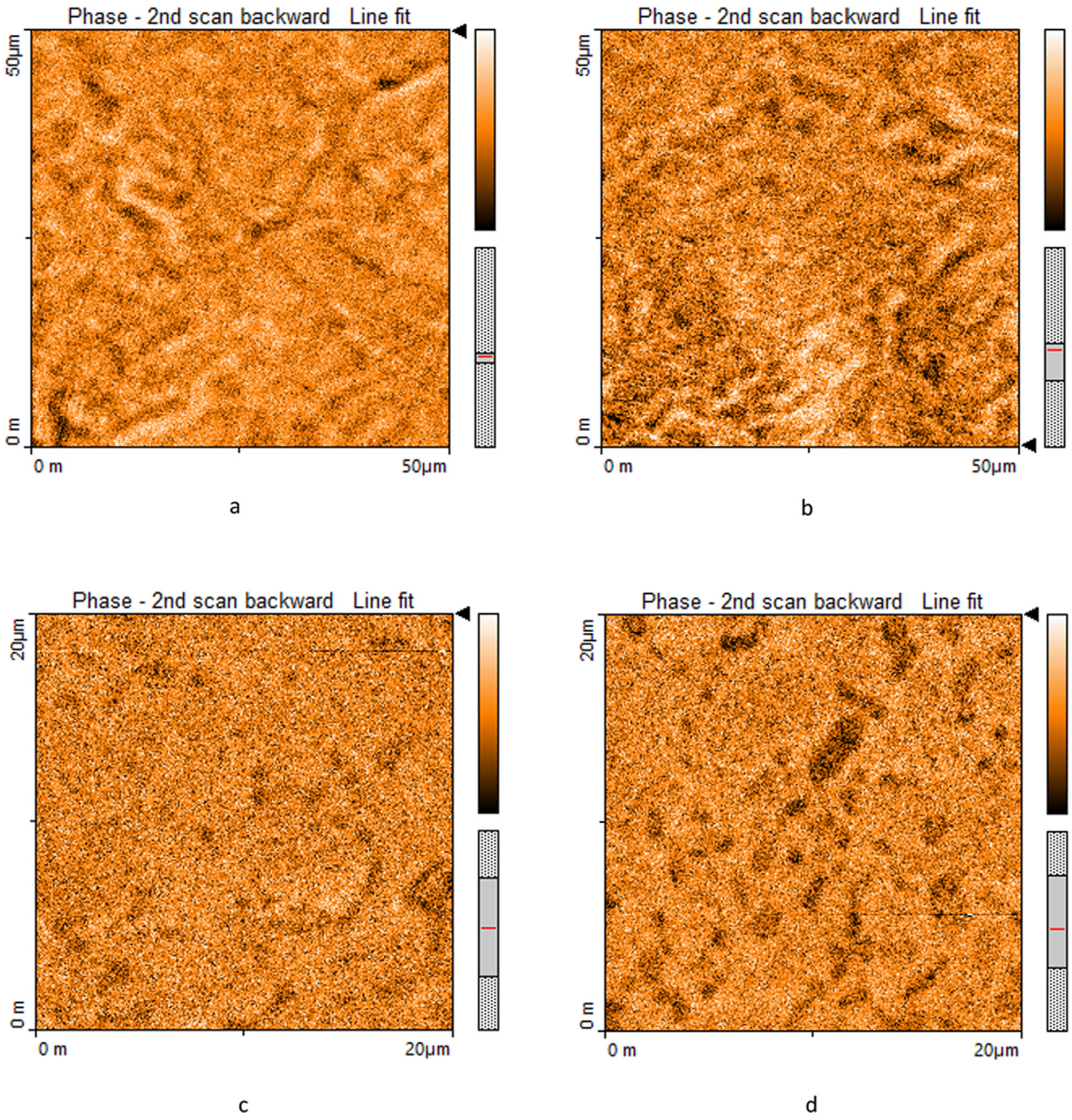

Fig. 8. MFM images of EN8 steel untreated (a) and AMF-treated (b) and NAB untreated (c) and AMF-treated (d) samples.

were evident. The uniform precipitation and dispersion of dislocations led to a more homogeneous microstructure and more uniform properties as shown by the lower mean-square deviation for the hardness and RS measurements. This is an important effect of the AMF treatment, as it is well-established that microstructural homogenisation in metals is especially important for increased resistance against cavitation erosion [45–49]. The conclusion concerning the formation of a more homogeneous structure after processing can be drawn from the analysis of the microstructure that reveals a lower level of dislocation entanglement, reduction of dislocation pile-ups and a more uniform distribution of dislocations. In addition, in the case of the EN8 steel, the MFM results show evidence of a more uniform distribution of magnetic domains, while the mean-square deviation of the results of the microhardness measurements is lower after treatment. To ensure accuracy of the microhardness results, 180 measurements were obtained per metal alloy per condition. Metal homogeneity (uniformity of microstructure) was further estimated from the coefficient of variation of hardness (CVH). Based on the data presented in Table 3, there was a general reduction of the CVH for EN8 steel, NAB, 70/30 brass and AA2014-T6 following the treatment. This indicates a general homogenisation of the alloy microstructure and an improvement in resistance to cavitation erosion.

The cumulative effect of all the above-mentioned factors (formation of compressive RS, precipitation strengthening, formation of clusters of Fe impurities and increased homogeneity of metal structure) has led to higher resistance to cavitation erosion for all the treated samples. As a result, while higher levels of erosion can be observed in the samples in the untreated condition, the treated samples exhibited surface characteristics of much lower cavitation erosion damage and surface roughness (refer to Figs. 4 – 7). As explained above, the driving force for these changes was the need to lower the Gibbs Free energy of the samples which were initially in a high-energy stressed/strained state. In addition, the

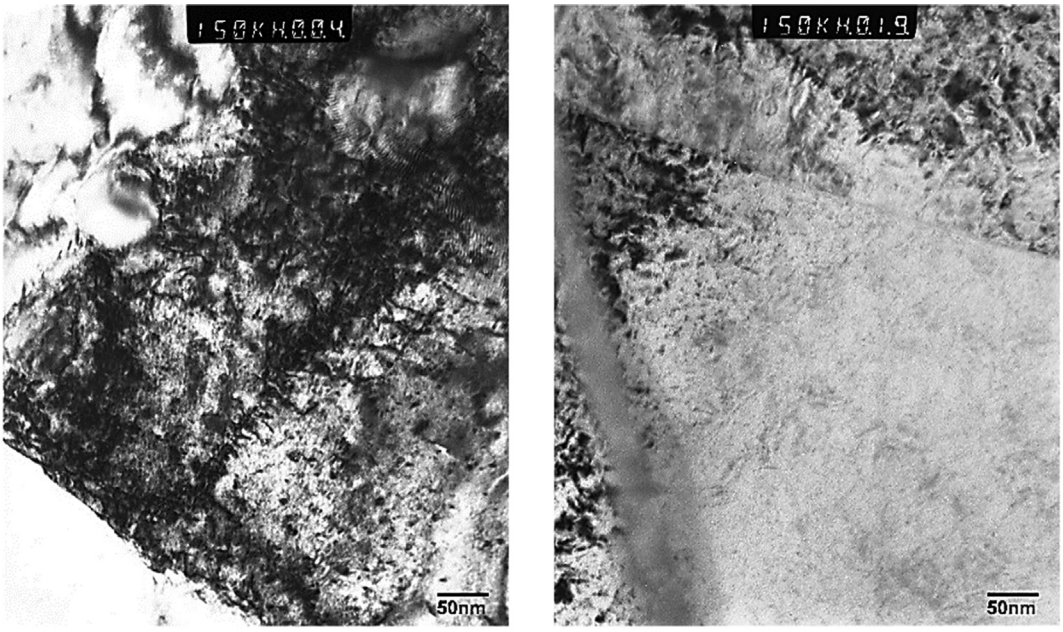

Fig. 9. TEM images of EN8 Steel untreated (a) and AMF-treated (b) samples.

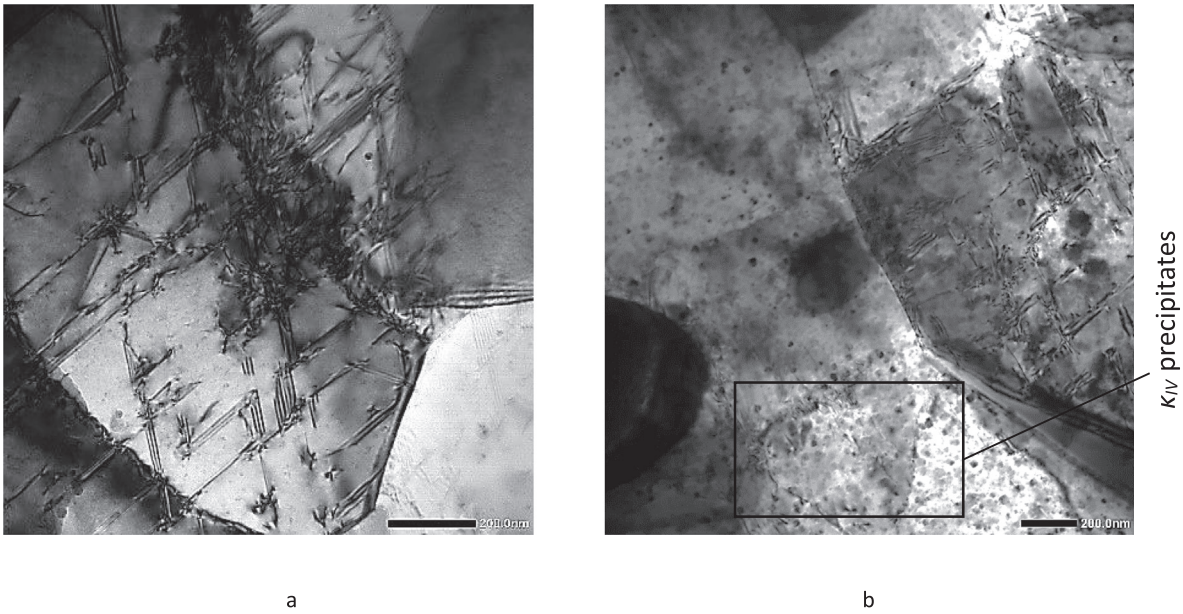

Fig. 10. TEM images of Nickel-Aluminium Bronze alloy untreated (a) and AMF-treated (b) samples.

contribution of the external magnetic field has led to the precipitation of strengthening phases and to the coalescence of iron impurities in the 70/30 brass alloy.

4.2.1. Effect of induced eddy currents

Numerical modelling has shown that eddy currents were induced at the surface of the samples with current densities ranging from 0.61×10^6 A/m^2 to 4.63×10^6 A/m^2 depending on the material and sample radius as shown in Table 5. The electric current itself can be considered as a parameter affecting the mechanical properties, particularly as it causes relaxation and redistribution of RS. This influence is based on the electroplastic effect which was observed experimentally for the first time by Troitskii [50] and was later widely investigated in other studies [51–55]. The observed results of the electroplastic effect were attributed to the influence of the electron wind of the current flow which props up dislocations, facilitating their movement and causing a drop in the resistance to deformation. This approach was based on the earlier theoretical work of Kravchenko [56] who had concluded that the electron flux creates an accelerating force for dislocations if the electron drift velocity exceeds the dislocation velocity. Later studies [51,57–59] showed that the "electron wind" approach was not able to explain the observed reduction in the resistance to deformation at the electric current densities used during real experiments. The same conclusion can be derived by applying the "electron wind" approach to the present experimental

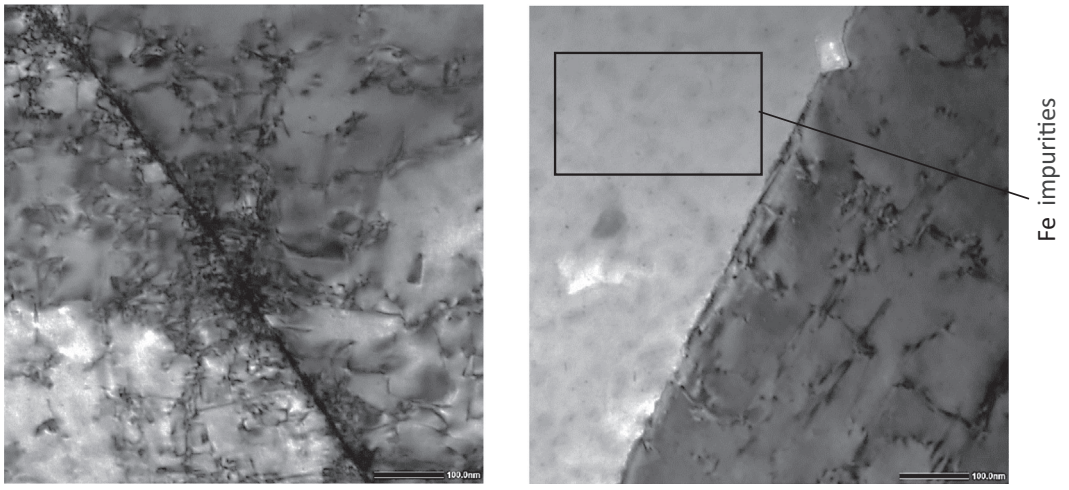

Fig. 11. TEM images of 70/30 brass alloy untreated (a) and AMF-treated (b) samples.

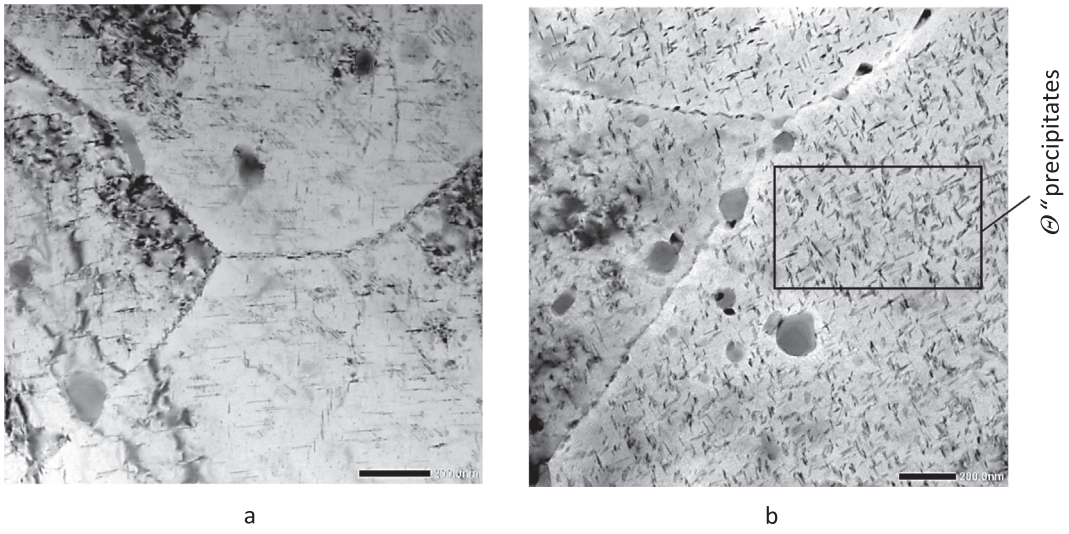

Fig. 12. TEM images of Aluminium Alloy 2014-T6 untreated (a) and AMF-treated samples (b).

work. Indeed, considering the basic relationships of the existing electrical conductivity theory [60], it is possible to determine the current density, i (A/m^2), the electric field intensity, E (V/m), and the electrical resistivity, ρ (Ω·m), from equations (4), (5) and (6):

$$\frac{dU}{dx} = E = \rho i \tag{4}$$

where

$$i = e v n_0 \tag{5}$$

$$\rho = 2m_e/(n_0 e^2 t_0) \tag{6}$$

and e is the electron elementary charge that is equal to 1.602 176634 × 10^{-19}C, v is the velocity of electron drift (m/s), n_0 is the number of conduction electrons per volume (m^{-3}), U is the electric potential (V), m_e is the electron rest mass that is equal to 9.10956 × 10^{-31} kg, and t_0 is the mean free time between electron ionic collisions.

Based on equations (4), (5) and (6), the kinetic energy of the electrons by the action of an electric field under isotropic scattering of electrons can be determined [61] as:

$$K_e = m_e v^2/2 = eE \cdot (v t_0) = \rho i (e v n_0) t_0/n_0 = \rho i^2 t_0/n_0 \tag{7}$$

At predetermined experimental conditions (of fixed i and ρ), the interaction between electrons and the crystal lattice for iron (EN8 steel), copper (70/30 brass and NAB) and aluminium (AA2014-T6) can be determined by equations (4) and (7). The increase in the kinetic energy of electrons in iron, copper and aluminium within their free path was calculated from equation (7) at the respective maximum current density values that were obtained from the numerical simulation. The results are presented in Table 5.

These values of ΔK_e are negligible in comparison with the change in the kinetic energy ΔK_T due to an increase in temperature T, by just 1 °C:

$$\Delta K_T \cong kT \cong 8.617\text{x}10^{-5} eV \tag{8}$$

where the Boltzmann constant is $k = 8.617333262145\,\text{x}10^{-5}\,eV \cdot K^{-1}$.

The alloy samples that were used in the present research had been cold-worked during manufacturing and were therefore in a strained condition. By taking a conservative estimate that the dislocation density, n_d, is about 10^{11}/cm^2, the ratio of the total density

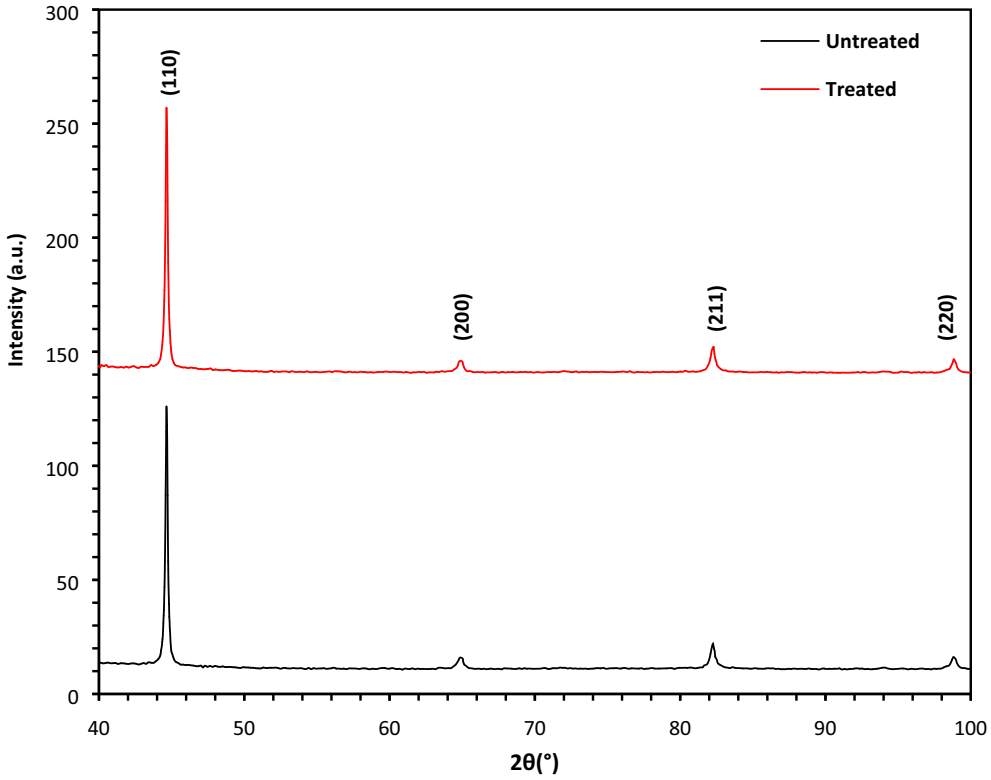

Fig. 13. XRD results for EN8 steel before and after AMF treatment showing no evidence of phase transformation.

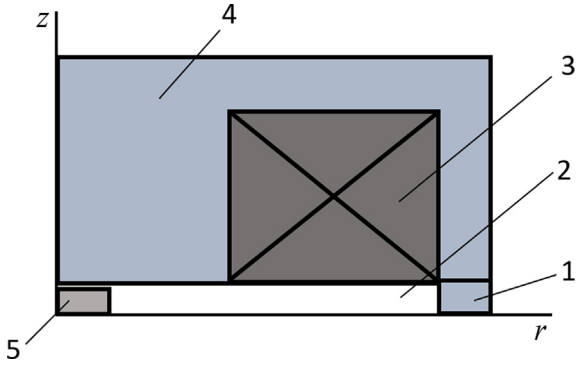

Fig. 14. Schematic presentation of magnetiser with sample (¼ model): 1 – steel spacer, 2 – air gap; 3 – winding (consists of 70 turns), 4 – core, 5 – sample.

of atoms, n, to the density of dislocations, n_d, for each alloy was calculated to be $n/n_{d(Fe)} = 1.94 \times 10^4$, $n/n_{d(Cu)} = 1.93 \times 10^4$ and $n/n_{d(Al)} = 2.16 \times 10^4$. The effective increase in the kinetic energy of atoms in dislocation cores due to electron wind can be estimated by equation (9):

$$\Delta K_{ef} = n/n_d \cdot \Delta K_e \quad (9)$$

In the case of EN8 steel, this value can be calculated as $\Delta K_{ef(Fe)} \cong 1.96 \times 10^{-16}$eV, for 70/30 brass $\Delta K_{ef(Cu)} \cong 1.01 \times 10^{-14}$ eV, for NAB $\Delta K_{ef(Cu)} \cong 4.42 \times 10^{-16}$eV and for AA2014-T6 $\Delta K_{ef(Al)} \cong 2.26 \times 10^{-15}$eV. Again, these values are still negligible in terms of thermally induced atomic motion based on equation (8). This means that the strength of the eddy currents is too low to induce atomic motion. From the above calculations, the direct interaction between the electron wind and dislocations is an unlikely cause of dislocation movement; it can therefore be concluded that the induced eddy currents were not the main reason for the observed microstructural changes. This conclusion can also be supported by results of other experimental research [62,63] where noticeable changes in the microstructure, mechanical properties and RS of metals took place only at electric current density values exceeding 10^8 A/m^2 [40].

4.2.2. Effect of magnetic field

It must be noted that in the present investigation, the applied treatment was carried out using a relatively "weak" magnetic field in comparison to other research by Golovin [64]. During the present investigation, the magnetic flux density, B, was 0.83 T and the energy, U_{mf}, of the magnetic field was estimated using equation (10) [64]:

$$U_{mf}\ \mu_b B \approx 4.8 \cdot 10^{-5} eV \quad (10)$$

Table 4
Physical properties of the materials used during modelling with QuickField 6 software.

Property	EN8 Steel sample	NAB	Brass	AA2014-T6	Core (steel)	Spacer (steel)	Winding wire (copper)	Air
Electrical Conductivity, MS/m	10	2.3	13.8	23	10	10	56	0
Relative permeability	B-H curve*	1.5**	1	1	B-H curve*	B-H curve*	1	1

The magnetic flux density vs magnetic field strength (B-H) curve for steel was taken from [39] and [31]**.

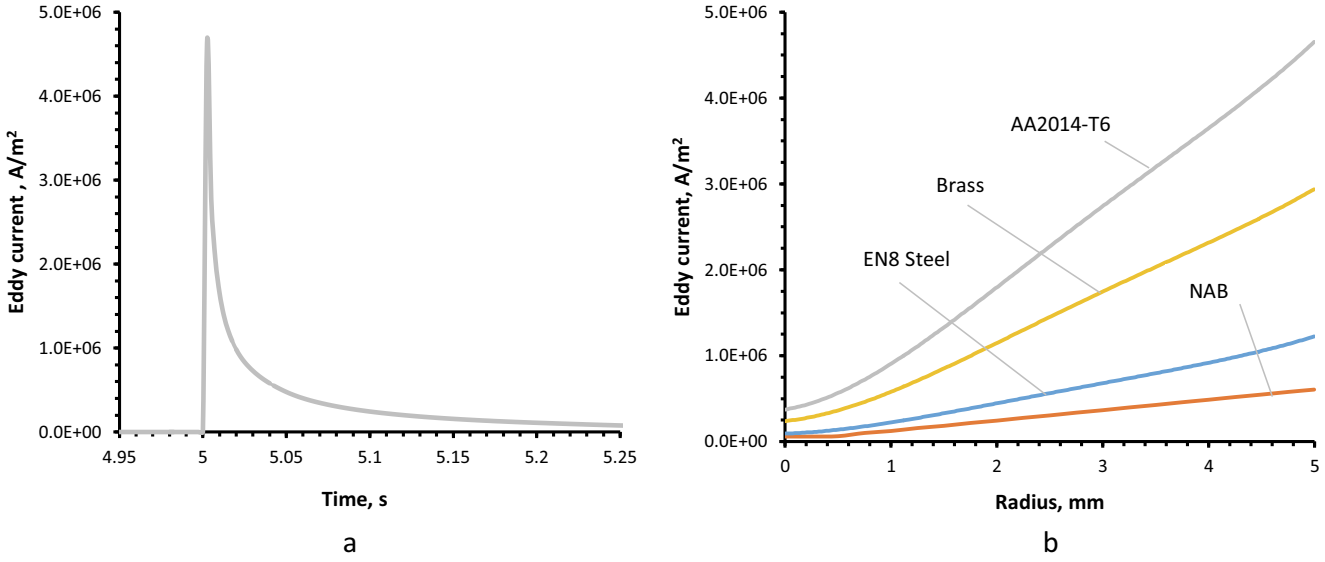

Fig. 15. Eddy current induced at the edge point of the AA2014-T6 sample (a) and distribution of maximum eddy currents vs radius on a flat surface of the samples (b).

Table 5
Current density and calculated Kinetic Energy of electrons by the action of an electric field for EN8 steel, NAB, 70/30 brass and AA2014-T6.

Alloy	EN8 steel	NAB	Brass	AA2014-T6
Current Density	1.22×10^6 A/m^2	0.61×10^6 A/m^2	2.92×10^6 A/m^2	4.63×10^6 A/m^2
Kinetic Energy	$\Delta K_{e(Fe)} \cong 1.01 \times 10^{-20}$ eV	$\Delta K_{e(Cu)} \cong 2.29 \times 10^{-20}$ eV	$\Delta K_{e(Cu)} \cong 5.24 \times 10^{-19}$ eV	$\Delta K_{e(Al)} \cong 1.05 \times 10^{-19}$ eV

where $\mu_b \approx 5.7883818012 \times 10^{-5}$ eV·T^{-1} and represents the Bohr magneton. At the same time the value of the kinetic energy, ΔK_T, at 20 °C (T_R = 293 K) can be estimated to be 2.5×10^{-2}eV from equation (8). This means that the energy of the magnetic field, U_{mf}, transferred to the metal samples during the treatment is three orders of magnitude lower than the kinetic energy of motion of the metal atoms at room temperature.

Based on literature data, some authors [64–67] have concluded that a weak magnetic field would trigger only limited mobility of dislocations, but further dislocation movement during treatment may occur due to the potential energy stored in the metals. Extra precipitation and coalescence of Fe impurities in the treated metals can also be the result of the triggering effect of the magnetic field on diffusional processes. In both cases, the application of the magnetic field is likely to trigger these microstructural changes to reduce the Gibbs Free energy. The specific mechanisms of influence of the magnetic field on metals leading to the observed changes at micro- and macro-levels will be discussed next for each alloy that was used in this Investigation.

EN8 steel. The changes in the EN8 steel microstructure following treatment can be related to the increased mobility of dislocations and to the release of stored strain energy leading to a reduction in the Gibbs Free energy. According to the simulation results, the steel samples were exposed to a magnetic flux density of 2.95 T. This value is sufficiently high enough to achieve full magnetic saturation of the steel accompanied by displacement of the magnetic domain walls. This has led to an increase in the size of the magnetic domains oriented parallel to the field by swallowing domains that are oriented opposite to it. The result of this is the creation of a single-domain structure. Alteration of the field during the treatment is accompanied by a decrease in the field down to a zero magnetic flux, thus increasing the number of magnetic domains. Further increase of the magnetic flux density of opposite polarity will again cause the displacement of the magnetic domain walls, finally leading to the creation of a single-domain structure at the point of magnetic saturation. This process is repeated throughout the entire treatment. As soon as this is completed (at zero magnetic flux density), the spontaneous division of the magnetic residual domains will lead to their final structure (see Fig. 8a and 8b).

The magnetic domain walls are pinned by dislocations [68] which form temporary barriers to their movement. However, when the magnetic flux density becomes high enough to overcome the local energy barrier at the dislocation, an abrupt displacement of the magnetic domain walls occurs and this is recorded in the form of Barkhausen noise [69]. The interaction between magnetic domain walls and dislocations can make it easier for the dislocations to overcome barriers in the crystal lattice. Depinning of dislocations caused by magnetic domain wall displacement due to domain increase/decrease and rotation and their additional movement driven by the stored energy is commonly suggested as the main mechanism of increased dislocation mobility in the case of magnetic treatment of ferromagnetic metals [22,70–72]. The magnetostriction of the metal volume due to the application of the magnetic field is also suggested as an extra factor triggering dislocation depinning [22,71].

NAB, 70/30 brass and AA2014-T6. In the case of the NAB bronze and the AA2014-T6 aluminium alloy, evolution of the microstructure takes place as a result of AMF treatment; this is represented by a more uniform distribution of dislocations and significant levels of precipitation, while in the case of 70/30 brass there is evidence of coalescence of iron impurity particles (Figs. 10 – 12). These changes are accompanied by a reduction in the Gibbs Free energy. As NAB has soft magnetic properties, the application of an external magnetic field with a magnetic flux density B = 0.83 T causes magnetization; according to the simulation results, a magnetic flux density of 1.18 T was applied leading to magnetisation. Similar to EN8 steel as discussed above, the alternating value of the magnetic field will cause gradual cyclic mag-

netic saturation of the metal and will build up larger magnetic domains within areas of the alloy with a higher concentration of the Fe_3Al and NiAl phases which are magnetic [73]. Following treatment, a new residual MFM domain pattern appeared (see Fig. 8c and 8d). Therefore, the same mechanism of dislocation depinning occurred as with EN8 steel involving the movement of magnetic domain walls due to domain increase/decrease and rotation. This action was driven by the stored energy in the as-received deformed NAB.

The model based on magnetic domain wall movement can be used to explain the unpinning of dislocations around the magnetic κ_I, κ_{II} and κ_{III} Fe_3Al and NiAl precipitates in NAB as they are relatively large in size [74]. However, the κ_{IV} precipitates which are also based on Fe_3Al [74] exhibit substantially different behaviour as they have significantly smaller size in comparison to the other κ phases. As shown in Fig. 10b, most of them have size ranging from 10 nm to 30 nm. As reported by Binns [75], magnetic particles of this size have a single-domain state in the absence of magnetisation and remain in this state during application of the magnetic field [76,77]. In this state, the particles have very high coercivity and consequently during reversing of magnetisation of the κ_{IV} phase, the widest possible hysteresis loop is achieved for a particle of that composition (Fe_3Al). This means that the external magnetic field does the greatest possible work on the metal and this work is dissipated as heat. This can lead to the unpinning of dislocations from these precipitates and to their additional motion due to the presence of stored energy (long-range stress and strain field). This heating is localized around the κ_{IV} precipitates and can enable diffusion mobility of "free" solute Fe and Al atoms that are present in the α solid solution and in the retained β-phase to form more κ_{IV} precipitates. Noting the extremely fine size of 10 nm to 30 nm of the κ_{IV} precipitates, the diffusion distance required for precipitation is likely to be small and therefore the level of localised heating is also likely to be small.

Another mechanism advancing diffusion mobility of solute Fe, Fe_3Al nuclei and small κ_{IV} precipitates is based on dipolar interaction causing an attraction or repulsion of magnetic dipoles. The energy levels of these interactions can be compared by considering a group of Fe atoms (Fe atom clusters), Fe_3Al nuclei or κ_{IV} precipitates of the same size and magnetic moment, m. When the magnetic field is applied, the magnetic moment of the dipoles (Fe atoms, their clusters, Fe_3Al nuclei and κ_{IV} precipitates) will be aligned with the direction of the field as shown in Fig. 16a. If the distance between two dipoles is r, the energy of the magnetic dipole interaction, E_D, can be expressed in this case as [78].

$$E_D = -\frac{\mu_0 m^2}{4\pi}\frac{3cos^2\theta - 1}{r^3} \quad (11)$$

where μ_0 is the vacuum magnetic permeability and θ is the angle between the y-axis and the radius-vector r. This equation shows that the energy of the magnetic dipole interaction, E_D, depends on the relative position of the interacting dipoles described by the geometric factor, f, where $f = \frac{3cos^2\theta-1}{r^3}$. Calculated values of the geometric factor, f, as a function of the relative position of the dipoles are presented in Fig. 16b.

The calculation of the geometrical factor, f, shows that the magnetic dipolar interaction energy E_D is negative and the dipoles are attracted to each other when two dipoles are on a line that coincides with the direction of the magnetic field. If two dipoles are oriented perpendicular to the field direction, the magnetic dipolar interaction energy, E_D, is positive and the dipoles repulse each other. Overall, the maximum energy of attraction is twice the maximum energy of repulsion. Under this condition, a higher diffusion mobility of Fe atoms, Fe atom clusters, Fe_3Al nuclei and nuclei of κ_{IV} precipitates can contribute to the formation of a larger number of κ_{IV} precipitates. Another source of κ_{IV} precipitates is the eutectoid transformation of the β phase to the copper-rich α-phase plus the κ eutectoid and further secondary κ precipitation based on Fe_3Al and NiAl.

In the case of 70/30 brass, the migration of dislocations from grain boundaries and the coalescence of Fe impurities were observed as a result of treatment as shown in Fig. 11. Similar to the effect on the NAB bronze, the AMF treatment has led to magnetization and has enhanced the presence of the ferromagnetic Fe impurities leading to the creation of greater Fe clusters which are observed in Fig. 11b. Considering that the size of the Fe clusters is quite similar to that for the κ_{IV} precipitates in NAB, it can be suggested that these Fe clusters also have a single-domain state and their re-orientation due to the application of the external magnetic field was accompanied by release of energy. It is obvious that the increased diffusion of Fe atoms together with the re-orientation of the Fe impurity clusters can violate the state of the dislocation pins and cause unpinning of dislocations which then moved under the action of the long-range stress and strain field stored in the material (in other words there was release of the stored energy). This movement leads to mutual annihilation of dislocations and to their re-arrangement as shown in Fig. 11b. The aluminium 2014-T6 alloy also experienced significant movement of dislocations away from grain boundaries and precipitation of the Θ'' phase due to treatment (Fig. 12). The aforementioned mechanisms that explain the observed effects of treatment are not applicable since the microstructure of this alloy contains no magnetic phases. Even if Fe is present as an impurity, it exists mainly in the form of $FeAl_2$ and $FeAl_3$ secondary phases [79] which are paramagnetic [80]. It should be noted that Al itself also is paramagnetic. At the same time, the paramagnetism of the main constituent phases

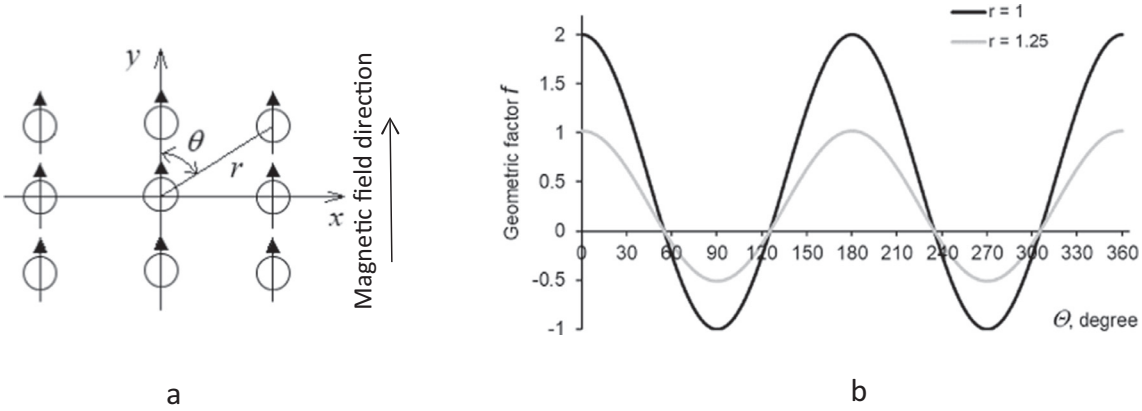

Fig. 16. Alignment of the dipoles under a magnetic field (a); variation of the geometrical factor f for $0 \leq \Theta \leq 360^0$ and for $r = 1$ and $r = 1.25$ (b).

can be a key point to understanding the effect of the magnetic field on the AA2014-T6 alloy in the present research. The most adequate model available to explain the observed changes in AA2014-T6 as caused by the magnetic field is presented in the work of Molotskii and co-workers [65,66]. The model assumes that the magnetic field changes the spin multiplicity of radical pairs formed by dangling bonds of dislocation nuclei and paramagnetic obstacles. As a result, the likelihood of depinning increases. According to Molotskii and his co-workers [65,66], a strong bond between atoms exists only in the ground singlet (*S*) state where the electron spins are antiparallel. In the excited triplet (*T*) state with parallel spins, the coupling is weaker or even absent. In the presence of a magnetic field, the *S*-to-*T* transition becomes possible and, as a result, the number of weaker *T* states in dislocation-obstacle systems (like dislocation-$FeAl_3$ pins or dislocation-forest dislocations) increases. This, in turn, makes possible the depinning of dislocations and their further annihilation and redistribution associated with their movement due to the release of stored energy (namely due to the long-range stress and strain field originally accumulated within the metal).

As for treatment-induced extra precipitation of the θ" phase, it should be mentioned that in the AA2014 aluminium alloy there is still a high level of solute Cu that is dissolved in the supersaturated solid solution (SSS) after the T6 temper. As above, it can be suggested that the magnetic field also increases the breakup of weaker *T* states in the Al- "free" solute Cu system leading to further increase in the diffusion mobility of Cu atoms. This results in secondary ageing accompanied by additional precipitation of GP-zones and further growth of existing and newly-formed GP-zones to the Θ" phase according to the precipitation sequence:

$$SSS \rightarrow GPzones \rightarrow \theta''$$

It must also be noted that the diffusion distance required to precipitate GP zones and Θ" is so small that this is possible at room temperature by natural ageing. The application of the external magnetic field was able to supply additional energy to enhance the precipitation process.

The models that were considered in this discussion on the influence of the alternating magnetic field on metals are not complete and exhaustive. It is clear that the influence of the magnetic field is more complex and may involve some other factors and mechanisms and this is the reason why complete understanding of this research topic is still a challenge. At the same time, it can be assumed that the main role of the magnetic field during the treatment is to trigger the transition from a metastable state to a more stable one by a decrease in the Gibbs Free energy. In order to further progress and commercialise this type of treatment, it is vital to develop equilibrium phase diagrams as a function of magnetic flux density. In addition, very little research has been conducted on the kinetics of the treatment. Consideration of the benefits of this treatment, for example, efficiency, simplicity and low energy consumption, it can be stated that further research is necessary to understand the mechanisms that lead to its effects.

5. Conclusions

In the present study, the effect of alternating magnetic field treatment on the cavitation erosion resistance of EN8 steel, NAB, 70/30 brass and 2014-T6 aluminium alloy was investigated through both numerical and experimental analyses. The following conclusions can be made:

1. Alternating magnetic field treatment had a non-thermal effect and led to significant improvement of the cavitation erosion resistance of all the investigated metals regardless of their magnetic nature (magnetic, diamagnetic and paramagnetic).

2. Two major groups of microstructural changes in the investigated alloys have been detected as a result of the AMF treatment; these microstructural changes involve (i) redistribution of dislocations, dispersion of dislocation tangles and pile-ups and reduction of the dislocation density near grain boundaries and, (ii) additional precipitation of secondary strengthening phases in NAB (κ_{IV} phase) and AA2014-T6 (GP zones and theta double prime, Θ") as well as formation of more iron clusters in 70/30 brass.

3. Due to the increased mobility of dislocations and additional precipitation and diffusion caused by the AMF treatment, a higher level of residual compressive stresses, increased hardness and higher homogenisation of the metal structure were achieved resulting in the improvement of the cavitation erosion resistance of all the investigated metals.

The mechanisms of increased dislocation mobility and precipitation after alternating magnetic field treatment for the alloys were different:

- in the case of EN8 steel, the main mechanism was related to magnetic domain wall movement as well as magnetostriction.
- in the NAB alloy, dislocation mobility and extra precipitation of the κ_{IV} phase were generated as a result of magnetic domain wall movement, cyclic re-magnetization of κ_{IV} precipitates and their dipolar interaction.
- in the case of 70/30 brass, dislocation mobility and formation of Fe impurity clusters was the result of cyclic re-magnetisation of Fe impurities and their dipolar interaction.
- for the AA2014-T6 alloy, dislocation mobility and extra precipitation of the theta double prime Θ" phase took place as a result of the change of the multiplicity of the radical pairs formed by cores of intersecting dislocations as well as dislocation cores and obstacles; this can also facilitate diffusion mobility of "free" solute Cu atoms from the aluminium super-saturated solution.

5. It is assumed that the main role of the alternating magnetic field during the treatment is to trigger a transition from a metastable state to a more stable one, accompanied by a decrease in energy that is originally stored in the alloys causing increased mobility of dislocations and extra precipitation and diffusivity.

This publication provides important results and insight on why the AMF treatment increases the mobility of dislocations and promotes precipitation of phases and leads to improvement in the cavitation erosion resistance. However, further research is still needed to fully understand the main mechanisms that stem from the influence of the magnetic field on structural metals.

Data availability

The authors are unable or have chosen not to specify which data has been used.

Declaration of Competing Interest

The authors declare that they have no known competing financial interests or personal relationships that could have appeared to influence the work reported in this paper.

Acknowledgements

This research was supported by the Marie Curie International Incoming Fellowship scheme within the 7th European Commission Framework Programme Grant number PIIF-GA-2010-274324 and by the CzechNanoLab Research Infrastructure supported by MEYS CR (LM2018110).

Anatolii Babutskyi reports financial support was provided by European Commission Seventh Framework Programme for Research and Technological Development People. Nada Pizurova reports financial support was provided by MEYS CR.

Data availability

The raw data required to reproduce these findings cannot be shared at this time as the data also forms part of an ongoing study. The processed data may be accessed in the Data in Brief document.

References

[1] S.S. Rajahram, T.J. Harvey, R.J.K. Wood, Erosion–corrosion resistance of engineering materials in various test conditions, Wear 267 (1) (2009) 244–254.
[2] A. Pola et al., Influence of ultrasound treatment on cavitation erosion resistance of AlSi7 alloy, Materials 10 (3) (2017) 256.
[3] A. Jayaprakash et al., Scaling study of cavitation pitting from cavitating jets and ultrasonic horns, Wear 296 (1) (2012) 619–629.
[4] S. Vaidya, C. Preece, Cavitation erosion of age-hardenable aluminum alloys, Metall. Trans. A 9 (3) (1978) 299–307.
[5] R. Fortes Patella et al., Mass loss simulation in cavitation erosion: Fatigue criterion approach, Wear 300 (1) (2013) 205–215.
[6] S.M. Ahmed, K. Hokkirigawa, R. Oba, Fatigue failure of SUS 304 caused by vibratory cavitation erosion, Wear 177 (2) (1994) 129–137.
[7] Y. Wang et al., The interaction mechanism of cavitation erosion and corrosion on HVOF sprayed NiCrWMoCuCBFe coating in artificial seawater, Appl. Surf. Sci. 525 (2020) 146499.
[8] X. Ding et al., Deposition and cavitation erosion behavior of multimodal WC-10Co4Cr coatings sprayed by HVOF, Surf. Coat. Technol. 392 (2020) 125757.
[9] I. Mitelea et al., Ultrasonic cavitation erosion of gas nitrided Ti–6Al–4V alloys, Ultrason. Sonochem. 21 (4) (2014) 1544–1548.
[10] W.J. Tomlinson, R.T. Moule, G.N. Blount, The effect of shot peening on the cavitation erosion of pure iron and austenitic stainless steel in distilled and 1% salt waters, Wear 118 (2) (1987) 233–242.
[11] L. Bao-Tong, Q. Sheng-Ru, S. Xiao-Yan, Exploration on repairing fatigue damage of steel specimens with magnetic treatment, Scr. Mater. 40 (7) (1999) 767–771.
[12] Y. Tang et al., Restoration of fatigue damage in stainless steel by high-density electric current, Int. J. Fatigue 56 (2013) 69–74.
[13] X. Yan, D. Yang, X. Liu, Influence of heat treatment on the fatigue life of a laser-welded NiTi alloy wire, Mater Charact 58 (3) (2007) 262–266.
[14] A. Babutskyi et al., Effect of electropulsing on the fatigue resistance of aluminium alloy 2014–T6, Mater. Sci. Eng. A 772 (2020) 138679.
[15] S. Akram et al., Effect of Alternating Magnetic Field on the Fatigue Behaviour of EN8 Steel and 2014–T6 Aluminium Alloy, Metals 9 (9) (2019) 984.
[16] M.A. Mohin et al., Effect of Electromagnetic Treatment on Fatigue Resistance of 2011 Aluminum Alloy, Journal of Multiscale Modelling 07 (03) (2016) 1650004.
[17] A. Babutskyi et al., Effect of pulsed magnetic treatment on the corrosion of titanium, Mater. Sci. Technol. 33 (12) (2017) 1461–1472.
[18] A. Babutskyi, A. Chrysanthou, C. Zhao, Effect of pulsed magnetic field pre-treatment of AISI 52100 steel on the coefficient of sliding friction and wear in pin-on-disk tests, Friction 2 (4) (2014) 310–316.
[19] T.A. Stolarski, Y. Makida, Influence of magnetic field on wear in high frequency reciprocating sliding contacts, Tribol. Int. 44 (9) (2011) 1004–1013.
[20] Z. Cai et al., Evaluation of effect of magnetostriction on residual stress relief by pulsed magnetic treatment, Mater. Sci. Technol. 20 (12) (2004) 1563–1566.
[21] X. Huang, Residual stress reduction by combined treatment of pulsed magnetic field and pulsed current, Mater. Sci. Eng. A 528 (19–20) (2011) 6287–6292.
[22] G. Tang et al., Effect of a pulsed magnetic treatment on the dislocation substructure of a commercial high strength steel, Mater. Sci. Eng. A 398 (1–2) (2005) 108–112.
[23] M. Hou et al., Effects of Pulsed Magnetic Fields of Different Intensities on Dislocation Density, Residual Stress, and Hardness of Cr4Mo4V Steel, Crystals 10 (2) (2020) 115.
[24] L. Gui-Rong et al., Influence of a high pulsed magnetic field on the tensile properties and phase transition of 7055 aluminum alloy, Mater. Res. Express 3 (10) (2016) 106507.
[25] J. Bockstedt, B.E. Klamecki, Effects of pulsed magnetic field on thrust bearing washer hardness, Wear 262 (9–10) (2007) 1086–1096.
[26] O. Bataineh, B. Klamecki, B.G. Koepke, Effect of pulsed magnetic treatment on drill wear, J. Mater. Process. Technol. 134 (2) (2003) 190–196.
[27] X. Xi, Y. Xia, Y. Hu, The Effects of Magnetic Treatment on the Tribological Behavior of AISI 1045 Steel under Lubricated Conditions, Tribol. Trans. 61 (4) (2018) 671–682.
[28] Y. Fahmy et al., Effects of a Pulsed Magnetic Treatment on the Fatigue of Low Carbon Steel, Scr. Mater. 38 (9) (1998) 1355–1357.
[29] F.P. Snegovskij, V.A. Uvarov, The influence of magnetic treatment of screw propeller on the cavitation wear, Trenie Iznos 3 (1991) 535–539.
[30] Asm.matweb.com, *ASM Material Data Sheet*.
[31] I. Richardson, Guide to nickel aluminium bronze for engineers, No. 222, Copper Development Association Publication, 2016.
[32] A. Standard, G32–10, Standard test method for cavitation erosion using vibratory apparatus, Annual Book of ASTM Standards, 1992, p. 3.
[33] Chahine, G.L., J.-P. Franc, and A. Karimi, Laboratory Testing Methods of Cavitation Erosion, in Advanced Experimental and Numerical Techniques for Cavitation Erosion Prediction, K.-H. Kim, et al., Editors. 2014, Springer Netherlands: Dordrecht. p. 21-35.
[34] Cseh, D. and V. Mertinger, *X-Ray Diffraction Measurements of Residual Stress Induced by Surface Compressing Methods*. Vol. 729. 2012. 199-204.
[35] Lewis, G.N. and M. Randall, *Thermodynamics and the free energy of chemical substances*. New York and London, 1923: McGraw-Hill.
[36] M.C. Gao et al., The effects of applied magnetic fields on the α/γ phase boundary in the Fe–Si system, J. Phys. D Appl. Phys. 39 (14) (2006) 2890–2896.
[37] W. Oliferuk, S.P. Gadaj, M.W. Grabski, Energy storage during the tensile deformation of armco iron and austenitic steel, Mater. Sci. Eng. 70 (1985) 131–141.
[38] G. Ravichandran et al., On the conversion of plastic work into heat during high-strain-rate deformation, in: AIP Conference Proceedings, American Institute of Physics, 2002, p. 620 557..
[39] Rao, D.K., *Properties of soft Magnetic Materials. Magnetic Materials Data.* Magweb, Version 7 Release Date Aug. 15, 2021.
[40] E. Vdovin, A. Kasumov, Direct observation of electrotransport of dislocations in a metal, Sov. Phys. Solid State 30 (1) (1988) 180–181.
[41] J. Frankel, A. Abbate, W. Scholz, The effect of residual stresses on hardness measurements, Exp. Mech. 33 (2) (1993) 164–168.
[42] J.I. Jang, Estimation of residual stress by instrumented indentation: A review, J. Ceram. Process. Res. 10 (3) (2009) 391–400.
[43] Z. Tong et al., Improvement in cavitation erosion resistance of AA5083 aluminium alloy by laser shock processing, Surf. Coat. Technol. 377 (2019) 124799.
[44] L. Zhang et al., Effects of laser shock processing on electrochemical corrosion resistance of ANSI 304 stainless steel weldments after cavitation erosion, Corros. Sci. 66 (2013) 5–13.
[45] C. Tang, F. Cheng, H.C. Man, Improvement in cavitation erosion resistance of a copper-based propeller alloy by laser surface melting, Surf. Coat. Technol. 182 (2–3) (2004) 300–307.
[46] C. Tang, F. Cheng, H. Man, Laser surface alloying of a marine propeller bronze using aluminium powder: Part I: Microstructural analysis and cavitation erosion study, Surf. Coat. Technol. 200 (8) (2006) 2602–2609.
[47] Z. Qin et al., Microstructure design to improve the corrosion and cavitation corrosion resistance of a nickel-aluminum bronze, Corros. Sci. 139 (2018) 255–266.
[48] S. Hanke et al., Cavitation erosion of NiAl-bronze layers generated by friction surfacing, Wear 273 (1) (2011) 32–37.
[49] Q. Song et al., Corrosion and cavitation erosion behaviors of friction stir processed Ni-Al bronze: effect of processing parameters and position in the stirred zone, Corrosion 70 (3) (2014) 261–270.
[50] O. Troitskii, Electromechanical effect in metals, J. Exp. Theor. Phys. 10 (1969) 18–22.
[51] Sprecher, A., S. Mannan, and H. Conrad, *Overview no. 49: On the mechanisms for the electroplastic effect in metals.* Acta Metallurgica, 1986. **34**(7): p. 1145-1162.
[52] K. Okazaki, M. Kagawa, H. Conrad, A study of the electroplastic effect in metals, Scr. Metall. 12 (11) (1978) 1063–1068.
[53] K. Okazaki, M. Kagawa, H. Conrad, Additional results on the electroplastic effect in metals, Scr. Metall. 13 (4) (1979) 277–280.
[54] H. Conrad, Electroplasticity in metals and ceramics, Mater. Sci. Eng. A 287 (2) (2000) 276–287.
[55] H. Krishnaswamy et al., Electroplastic behaviour in an aluminium alloy and dislocation density based modelling, Mater. Des. 124 (2017) 131–142.
[56] V.Y. Kravchenko, Effect of directed electron beam on moving dislocations, Sov. Phys. JETP 24 (6) (1967) 1135–1142.
[57] H. Conrad, A.F. Sprecher, F.R.N.E. In Nabarro, Dislocations in Solids, Elsevier Science Publishers B.V, Amsterdam, The Netherlands, 1989, p. 499.
[58] V. Spytsin, O. Troitsky, Electroplastic Deformation of Metals, Nauka, Moscow, 1985.
[59] V. Fiks, Interaction of conduction electrons with single dislocations in metals, Soviet Physics JETP 53 (1981) 1209.
[60] R.W. Christy, A. Pytte, The structure of matter: an introduction to modern physics, WA Benjamin, 1965.
[61] A. Babutskyi et al., Effect of pulsed magnetic treatment on the corrosion of titanium, Mater. Sci. Technol. (2017) 1–12.
[62] Y.V. Baranov et al., Physical bases of electric-pulse and electroplastic treatments and new materials, Chap 1 (2001) 56–77.
[63] Troitskii, O., et al., *Application of high-density current in plastic working of metals.* physica status solidi (a), 1979. **52**(1): p. 85-93.
[64] Y.I. Golovin, Magnetoplastic effects in solids, Phys. Solid State 46 (5) (2004) 789–824.
[65] M. Molotskii, V. Fleurov, Spin effects in plasticity, Phys. Rev. Lett. 78 (14) (1997) 2779.
[66] M. Molotskii, Possible mechanism of the magnetoplastic effect, Soviet physics. Solid state 33 (10) (1991) 1760–1761.
[67] M.I. Molotskii, Theoretical basis for electro-and magnetoplasticity, Mater. Sci. Eng. A 287 (2) (2000) 248–258.
[68] Jiles, D., *Introduction to magnetism and magnetic materials*. 2015: CRC press.
[69] Y. Fukumoto, A. Kamijo, Effect of milling depth of the junction pattern on magnetic properties and yields in magnetic tunnel junctions, Jpn. J. Appl. Phys. 41 (2B) (2002) L183.

[70] A. Çelik et al., Effect of magnetic treatment on fatigue life of AISI 4140 steel, Mater. Des. 26 (8) (2005) 700–704.
[71] B.E. Klamecki, Residual stress reduction by pulsed magnetic treatment, J. Mater. Process. Technol. 141 (3) (2003) 385–394.
[72] S. Wu et al., A micro-mechanism model of residual stress reduction by low frequency alternating magnetic field treatment, J. Mater. Process. Technol. 132 (1) (2003) 198–202.
[73] R.D. Shull, H. Okamoto, P.A. Beck, Transition from ferromagnetism to mictomagnetism in Fe—Al alloys, Solid State Commun. 20 (9) (1976) 863–868.
[74] R.J. Wood, Marine wear and tribocorrosion, Wear 376 (2017) 893–910.
[75] Binns, C., *Introduction to nanoscience and nanotechnology*. Vol. 14. 2010: John Wiley & Sons.
[76] E.C. Stoner, E. Wohlfarth, *A mechanism of magnetic hysteresis in heterogeneous alloys.* Philosophical Transactions of the Royal Society of London, Series A, Mathematical and Physical Sciences 240 (826) (1948) 599–642.
[77] E. Wohlfarth, Hard magnetic materials, Adv. Phys. 8 (30) (1959) 87–224.
[78] Y. Zhang et al., Grain boundary characteristics and texture formation in a medium carbon steel during its austenitic decomposition in a high magnetic field, Acta Mater. 53 (19) (2005) 5213–5221.
[79] Belov, N.A., A.A. Aksenov, and D.G. Eskin, *Iron in aluminium alloys: impurity and alloying element*. 2002: CRC Press.
[80] L. Mondolfo, Aluminum Alloys: Structure and Properties, Butterworths, London/Boston. (1976).